Geochimica et Cosmochimica Acta 343 (2023) 180–195

Contents lists available at ScienceDirect

Geochimica et Cosmochimica Acta

journal homepage: www.elsevier.com/locate/gca

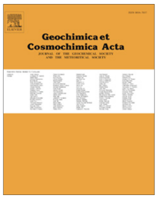

Mineralogical, magnetic and geochemical data constrain the pathways and extent of weathering of mineralized sedimentary rocks

Sergio Carrero [a,b,c], Sarah P. Slotznick [b,d], Sirine C. Fakra [e], M. Cole Sitar [a], Sharon E. Bone [f], Jeffrey L. Mauk [g], Andrew H. Manning [g], Nicholas L. Swanson-Hysell [b], Kenneth H Williams [a,h], Jillian F. Banfield [a,b], Benjamin Gilbert [a,b,*]

[a] *Energy Geoscience Division, Lawrence Berkeley National Laboratory, Berkeley, CA 94720, USA*
[b] *Department of Earth and Planetary Science, University of California, Berkeley, CA 94720, USA*
[c] *Institute of Environmental Assessment and Water Research, (IDAEA-CSIC), Jordi Girona 18-26, 08034 Barcelona, Spain*
[d] *Department of Earth Sciences, Dartmouth College, Hanover, NH 03755, USA*
[e] *Advanced Light Source, Lawrence Berkeley National Laboratory, Berkeley, CA 94720, USA*
[f] *SLAC National Accelerator Laboratory, Menlo Park, CA 94025, USA*
[g] *US Geological Survey, Denver, CO 80225, USA*
[h] *Rocky Mountain Biological Lab, Gothic, CO 81224, USA*

ARTICLE INFO

Article history:
Received 1 March 2022
Accepted 9 November 2022
Available online 11 November 2022
Associate editor: Lixin Jin

Keywords:
Rock Weathering
Magnetism
High-resolution X-ray fluorescence
Weathering models

ABSTRACT

The oxidative weathering of sulfidic rock can profoundly impact watersheds through the resulting export of acidity and metals. Weathering leaves a record of mineral transformation, particularly involving minor redox-sensitive phases, that can inform the development of conceptual and quantitative models. In sulfidic sedimentary rocks, however, variations in depositional history, diagenesis and mineralization can change or overprint the distributions of these trace minerals, complicating the interpretation of weathering signatures. Here we show that a combination of bulk mineralogical and geochemical techniques, micrometer-resolution X-ray fluorescence microprobe analysis and rock magnetic measurements, applied to drill core samples and single weathered fractures, can provide data that enable the development of a geochemically consistent weathering model.

This work focused on one watershed in the Upper Colorado River Basin sitting within the Mesaverde Formation, a sedimentary sandstone bedrock with disseminated sulfide minerals, including pyrite and sphalerite, that were introduced during diagenesis and subsequent magmatic-hydrothermal mineralization. Combined analytical methods revealed the pathways of iron (Fe), carbonate and silicate mineral weathering and showed how pH controls element retention or release from the actively weathering fractured sandstone. Drill core logging, whole rock X-ray diffraction, and geochemical measurements document the progression from unweathered rock at depth to weathered rock at the surface. X-ray microprobe analyses of a 1-cm size weathering profile along a fracture surface are consistent with the mobilization of Fe(II) and Fe(III) into acidic pore water from the dissolution of primary pyrite, Fe-sphalerite, chlorite, and minor siderite and pyrrhotite. These reactions are followed by the precipitation of secondary minerals such as of goethite and jarosite, a Fe-(oxyhydr)oxide and hydrous Fe(III) sulfate, respectively. Microscale analyses also helped explain the weathering reactions responsible for the mineralogical transformations observed in the top and most weathered section of the drill core. For example, dissolution of feldspar and chlorite neutralizes the acidity generated by Fe and sulfide mineral oxidation, oversaturating the solution in both Fe-oxides. The combination of X-ray spectromicroscopy and magnetic measurements show that the Fe(III) product is goethite, mainly present either as a coatings on fracture surfaces in the actively weathering region of the core or more homogeneously contained within the unconsolidated regolith at the top of the core. Low-temperature magnetic data reveal the presence of ferromagnetic Fe-sulfide pyrrhotite that, although it occurs at trace concentrations, could provide a qualitative proxy for unweathered sulfide minerals because the loss of pyrrhotite is associated with the onset of oxidative weathering. Pyrrhotite loss and goethite formation are detectable through room-temperature magnetic coercivity changes, suggesting that rock magnetic measurements can determine weathering intensity in rock samples at many scales. This work contributes evidence that the weathering of sulfidic sedimentary rocks follows a geochemical pattern in which the abundance of sulfide minerals controls the generation of acidity and dissolved elements, and the pH-dependent mobility of these elements controls their export to the ground- and surface-water.

---

* Corresponding author at: Energy Geoscience Division, Lawrence Berkeley National Laboratory, Berkeley, CA 94720, USA.
E-mail address: bgilbert@lbl.gov (B. Gilbert).

https://doi.org/10.1016/j.gca.2022.11.005
0016-7037/

1. Introduction

Rock weathering transforms competent bedrock into unconsolidated regolith, initiating soil formation, and releasing elements into groundwater. Weathering proceeds through rock fracturing and a sequence of chemical reactions between rock minerals and water, solutes and atmospheric and subsurface gases. These reactions play an important role in elemental cycles controlling not only element mobility between bedrock and ground or surface water, but also the consumption and potential release of CO_2 depending on the lithology (Kump et al., 2000; Dessert et al., 2003; Hilton and West, 2020) Many factors affect the rates and consequences of rock weathering. Tectonic setting plays a role because high rates of uplift in mountainous regions are associated with high rates of erosion and weathering (Gaillardet et al., 1999; West et al., 2005). Bedrock lithology plays a role with different weathering rates and potential for CO_2 consumption or release for carbonate, shale, or sandstone sedimentary rocks (Meybeck, 1987; Hubbard et al., 2018). The presence of sulfide minerals has a major influence on weathering and watersheds because the oxidative dissolution of sulfide minerals generates acidity that can accelerate mineral dissolution and mobilize metals into freshwater (Gray, 1998; Blodau, 2006; Nordstrom, 2011; Tuttle et al., 2014).

Many watersheds in the Upper Colorado River Basin overlap the Colorado Mineral Belt, which is a northeast-trending, ~500 km-long, 25–50-km wide belt of Late Cretaceous to Paleogene plutons and hydrothermal mineral deposits (e.g., Alford et al., 2020; Chapin, 2012; Tweto and Sims, 1963) (Fig. S1). Decadal trends in increasing sulfate concentrations in stream and lake waters reflect climate sensitivity of the weathering of sulfidic rock in some parts of the Rocky Mountains (Mast et al., 2011; Manning et al., 2013), which may increase the release of contaminants such as arsenic (As) (Bondu et al., 2016). Differences in stream chemistry across catchments varying in lithology have illustrated the importance of bedrock composition on acid rock drainage and its impacts on water resources (Verplanck et al., 2009). However, more detailed knowledge of the weathering pathways is necessary for the development of conceptual and quantitative models for weathering sensitivity to temperature and runoff (Manning et al., 2013; Sullivan et al., 2019).

Weathering overprints the host rock with records of mineral reactions, especially reactions involving redox-sensitive phases. These records are generally characterized at the meter scale in more homogeneous lithologies and can be interpreted to generate models for weathering pathways and element export (Brantley and Lebedeva, 2011). In mineralized sedimentary rocks, however, larger-scale weathering patterns can be challenging to identify from bulk observations due to sharp variations in mineralogy and rock chemistry imposed by complex depositional, diagenetic, metamorphic, and mineralization histories. In competent rocks with low permeability, however, weathering mainly occurs around rock fractures, and penetrates a few millimeters into the rock (Gu et al., 2020). At this smaller scale, the bedrock composition is more uniform and hence millimeter-to-centimeter-scale weathering records may provide clearer depictions of the chemical reactions involved in the transformation of unweathered rock (farther from the fracture) to weathered rock (at the fracture). Once these reactions have been well characterized, they may be extrapolated to understand the weathering record throughout the more complex mineralized rock profile.

Here we apply meter- and microscale mineralogical and chemical analyses to reveal the sequence of mineralogical transformations and infer the controls on element mobilization and retention within a weathered fracture surface in a hydrothermally altered sandstone from the Redwell Basin, CO. Microfocused X-ray fluorescence spectromicroscopy methods provide the distribution and chemical speciation of major and trace elements in heterogeneous Earth systems (Manceau et al., 2002; Toner et al., 2016) and on mineral changes during weathering reactions (Buss et al., 2008; Bao et al., 2022). Herndon et al. (2014) focused on Mn mobility using micro X-ray fluorescence (μXRF) mapping and micro X-ray adsorption near edge structure (μXANES) spectroscopy to reveal the distribution and speciation of Mn released by shale weathering at the Shale Hills Critical Zone Observatory, PA, USA. Our work expands on these directions with a focus on Fe and sulfide mineralogy.

Transformations of Fe-minerals are critical reactions in sulfidic rock weathering but can be challenging to determine by either bulk methods or microchemical studies because the products of sulfide minerals oxidation are typically fine-scale phases at low abundance. Rock magnetic methods can identify Fe-bearing ferromagnetic minerals that are (sub)microscale and at low concentration in rock, and the measurements can be made from sub-centimeter-sized samples. Magnetic methods have been widely applied to soils, paleosols, and sediments to reveal paleoclimate and environmental redox states (Maher and Thompson, 1992; Liu et al., 2012; Slotznick et al., 2018, 2019). There are few studies applying rock magnetic data to constrain the weathering of sulfidic rock (e.g., Chevrier et al., 2006; Essalhi et al., 2011). In this study, we integrate whole rock geochemical data with microfocused X-ray fluorescence spectromicroscopy, magnetic methods, and scanning electron microscopy (SEM) data to develop a conceptual model of the key geochemical and mineralogical transformations associated with weathering and element release pathways throughout the Redwell Basin.

2. Materials and methods

2.1. Site description

Redwell Basin, in south-central Colorado, USA, is a small alpine hanging glacial valley located in the Upper Colorado River Basin at an elevation of ~3300 m (Fig. 1). The bedrock of the basin is a thick transitional package of late Cretaceous marine mixed shales (Mancos Shale) to marginal marine mixed sandstone and shale (Mesaverde Formation) (Gaskill et al., 1967). The basin was intruded 15.767 ± 0.028 million years ago by a porphyritic granite stock that hosts the Mt. Emmons porphyry Mo deposit (Thomas and Galey, 1982; Rosera et al., 2021). The associated hydrothermal activity formed a near-surface stockwork deposit consisting of veins filled by quartz, feldspar and sulfide minerals (Sharp, 1978). The Daisy Mine and other small workings in Redwell Basin exploited polymetallic veins; these mines are now inactive (Fig. 1).

The Redwell Basin drains to the Redwell Creek, a tributary of the Gunnison River, which is an important source of drinking and irrigation water in the area. In the highest-altitude reach of Redwell Creek, the water pH is circumneutral, but downstream inputs of surface and subsurface waters affected by the oxidative weathering of sulfide minerals lower the pH to below 4 and increase the concentration of Zn and other metals (Verplanck et al., 2004; Kimball et al., 2010). Mixing analysis indicates that ~3/4 of the Zn and ~1/2 of the dissolved sulfate originate from mining-related activities that exposed sulfidic rock to oxygenated fluids (Wanty et al., 2004).

A 50 m core (MW1) was drilled in 2017 at 3404 m elevation (Figs. 1 and S2), above the start of perennial flow in Redwell Creek, higher than mining activities near the Daisy Mine. This core is stored in the USGS Core Research Center in Lakewood, CO.

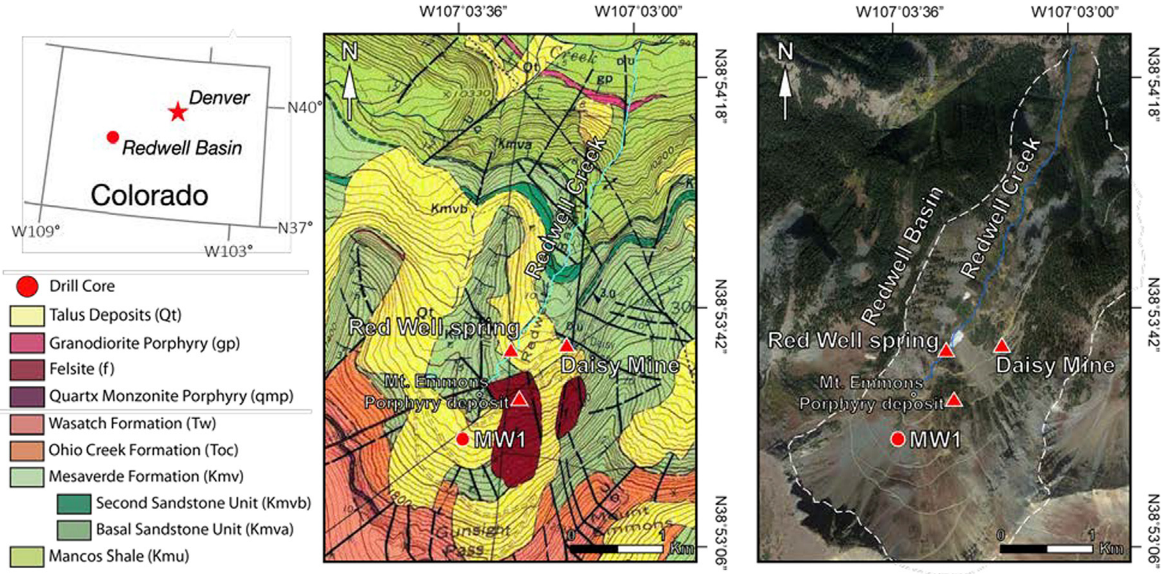

Fig. 1. Geographic location of Redwell Basin in Colorado, USA. Geological and topographical map of the basin (Gaskill et al., 1967) showing location of the MW1 drill site, the Red Well spring, Redwell Creek, Mt. Emmons Porphyry deposit, and the Daisy Mine. Satellite image (Google Earth) showing the boundary of Redwell Basin. (For interpretation of the references to color in this figure legend, the reader is referred to the web version of this article.)

2.2. Rock Sampling and Sample Preparation

Samples were collected from the MW1 core at approximately 0.5 m intervals between the upper part of the core and 13 m below ground surface (bgs), and every 3 m between 13 m and 45 m bgs, to obtain chemical and mineralogical depth profiles. All samples were collected from core with moderate to low concentrations of hydrothermal mineralization; veins filled by sulfide minerals and areas with high visible concentrations of disseminated sulfide minerals were avoided. A second group of samples were collected from the first 10 m of core where weathering could be identified around fractures on the rock by changes in color or texture (Fig. S2). The weathering profiles were revealed by cuts perpendicular to the fracture surfaces and were made into thin sections for microfocused X-ray spectromicroscopy and optical and electron microscopy. In addition, several 2-mm-thick slices were cut parallel to the fracture surface for rock magnetic analysis of layers representing weathered (fracture surface) and unweathered zones.

2.3. Analytical Techniques

2.3.1. Elemental analyses

Bulk samples were analyzed for major and trace elements quantification in the laboratory of ALS Global (Reno, NV). Major components (SiO_2, Fe_2O_3, Al_2O_3, CaO, MgO, Na_2O, K_2O, Cr_2O_3, TiO_2, MnO, P_2O_5, SrO and BaO) were analyzed following the method ME-IPC06, whereas trace elements were analyzed by methods ME-MS81 (Ba, Ce, Cr, Cs, Dy, Er, Ga, Gd, La, Sn, Sr, U, V, W, Y, Yb, Zr), ME-MS42 (As, Hg, Sb, Se) and ME-4ACD81 (Ag, Cd, Co, Cu, Ni, Pb, Sc, Zn). In all these methods, rock samples were melted in lithium borate and digested in aqua regia, following an Inductively Coupled Plasma Atomic Emission Spectroscopy (ICP-AES) analysis, for ME-IPC06 and ME-4ACD81, or Inductively Coupled Plasma Mass Spectroscopy (ICP-MS), for ME-MS42 and ME-MS81. Carbon and S were analyzed by combustion and infrared detection according to the methods C-IR07 and S-IR08, respectively. We assume that the C is inorganic C because the drill core is typically light green to light gray sandstone and contains no visible organic material. Mass balance constraints indicate that all C in 78% of the samples could be accounted for by Ca-Mg-Mn carbonate minerals, and the remaining 22% may contain 0.04 to 0.35 wt% organic C. Detection limits were 0.01% in weight for major elements (Al, C, Ca, Cr, Fe, K, Mg, Na, P, S, Si, Sr, Ti) and 10 ppb for As, Cr and Cu; 1 ppb for Cd; 100 ppb for Mn, Se and Zn; 40 ppb for Ni; and 5 ppb for Pb; with an analytical error lower than 5%. The mass transfer coefficient (τ) was calculated to assess the elemental profile and the relative change in concentration due to changes in other elements in the rock, according to the following equation (Brimhall and Dietrich, 1987; Anderson et al., 2002):

$$\tau_{i,j} = \frac{C_{j,w} C_{i,p}}{C_{j,p} C_{i,w}} - 1 \tag{1}$$

where $C_{j,w}$ and $C_{j,p}$ indicate the concentration of the element j in the weathered and parent samples, respectively, and $C_{i,w}$ and $C_{i,p}$ are the concentration of the immobile element (Zr in this case) in the weathered and parent sample, respectively. Positive $\tau_{i,j}$ values indicate enrichment of the element j, and negative values indicate depletion with respect to the parent (in our case sample at 12.1 m bgs). The parent reference sample was chosen based on no weathering reactions noted in hand sample observation and low or no mineralization according to Zr concentration (<400 ppm, natural break in the core between mineralized and not mineralized samples). The sample at 12.1 m bgs achieves these requirements and also displays relatively immobile elemental concentrations close to the median value of the population (e.g., element, median, sample: SiO_2 % 70.7 vs 70.7; TiO_2 % 0.5 vs 0.48; or Zr ppm 228 vs 300).

2.3.2. X-ray diffraction

2.3.2.1. Clay mineral Analysis. The clay fraction was extracted from bulk samples to assess the clay mineral composition and abundance, following the protocol described by Moore and Reynolds (1997). The principal steps are: (1) placing 10 g of ground rock into 40-mL polycarbonate centrifuge tubes and adding Milli-Q water at a solid to liquid ratio of 1:10 (by weight), (2) sonicating in three cycles of 30 min for cement dissolution and clay mineral desegregation, (3) leaching with oxalic acid (0.1 M) for Fe-oxide dissolution; (3) addition of sodium pyrophosphate (1 mM) as a clay mineral dispersive agent and sonicating again; (5) decantation to remove particles >2 μm, waiting 4 h and carefully removing the first 5 cm where all suspended particles are <2 μm. To quantify the total clay mineral proportion, step 5 was repeated as many times as needed until the first 5 cm of supernatant were totally clear of suspended particles. The remnant non-clay fraction was washed in Milli-Q water several times, dried at room temperature and weighed. The mass of the clay fraction was calculated from the difference in weight between steps 1 and 5.

2.3.2.2. Data acquisition. The mineralogical composition of rock samples were analyzed using XRD (Chung, 1974) on a Rigaku SmartLab high-resolution XRD diffractometer using Bragg-Brentano geometry. The diffractometer was equipped with a theta-theta goniometer and a rotating sample holder using Cu ($\lambda_{k\alpha1}$ = 1.5406 Å and $\lambda_{k\alpha2}$ = 1.5444 Å) cathode. For clay mineral identification, an aliquot from the <2 μm particle size suspension was dropped on a zero-background plate and dried at room temperature to obtain oriented clay mineral samples. Bulk rock was ground, obtaining a fine homogeneous powder, and placed in an aluminum holder to ensure random particle orientations. Bulk rock sample data were collected from 2 to 90°2θ with a 0.02°2θ step-size and count times of 2 s per step. Oriented clay mineral samples were measured (3 to 25 and 3 to 75°2θ with 0.02°2θ step-size and 10 and 2 s per step, respectively) under four different conditions: (1) dry at room temperature, (2) saturated with ethylene–glycol for 1 h at 333 K, (3) heated at 673 K for 1 h, and (4) heated at 823 K for 1 h. The diffraction patterns were analyzed using the software Match! (Putz and Brandenburg, 2011) and the PDF-2 mineral database (Gaste-Rector and Blanton, 2019).

2.3.3. Scanning electron microscopy

A scanning electron microscopy (SEM) instrument (Zeiss Evo LS10) equipped with an energy-dispersive X-ray spectroscopy (EDX) detector was used to analyze gold-coated rock thin sections. Back-scatter electron (BSE) imaging with the SEM was performed using a 5.0 kV accelerating voltage and 1.5 μm spot size. EDX was performed at 30 kV using a 3.0 μm spot size. Semi-quantitative chemical analyses by EDX provide an approximate stoichiometric composition, allowing mineral identification.

2.3.4. Synchrotron X-ray spectromicroscopy.

μXRF imaging and μXANES spectroscopy were performed on XFM beamline 10.3.2 at the Advanced Light Source (ALS, Berkeley, CA, USA, Marcus et al., 2004) for tender- and hard-X-ray analysis and on beamline 2–3 at the Stanford Synchrotron Radiation Light Source (SSRL, USA) for hard-X-ray analysis.

At ALS beamline 10.3.2, μXRF mapping and μXANES were performed under ambient conditions. All data were recorded with a single element silicon drift fluorescence detector (Amptek FAST XR-100SDD). μXRF elemental maps (S, P, Si, Al) were collected at 2700 eV (~230 eV above the S K-edge) using a 20 × 20 μm pixel size and a beam spot size of 4 × 4 μm. μXRF spectra were simultaneously collected on each pixel of the maps. All maps were then deadtime-corrected, and element interferences removed using custom LabVIEW 2018 (National Instruments, Austin, TX, USA) software available at the beamline (xraysweb.lbl.gov/uxas/Databases/Overview.htm). Elemental maps were then analyzed with a MatlabR2020b routine available at beamline 10.3.2. μXRF spectra were recorded at 10 keV at specific locations on the maps. Sulfur K-edge μXANES spectra were recorded for areas with high S concentration and low or high correlation with other elements, according to statistical PCA analysis. Spectra were recorded by continuously scanning the Si (1 1 1) monochromator (Quick XAS mode) in the 2450 to 2550 eV range, with 0.2 eV steps around the edge. These spectra were then background-subtracted using a spectrum recorded in air (sample out). Spectra were subsequently deadtime corrected, deglitched, calibrated, pre-edge background subtracted and post-edge normalized using custom LabVIEW 2018 software available at 10.3.2. Spectra were calibrated using gypsum ($CaSO_4$), with its main peak (white line) set at 2482.75 eV. Sulfur K-edge μXANES of mineral standards (jarosite and sphalerite) were obtained from the S XANES mineral database of the European Synchrotron Radiation Facility ID21 beamline.

μXRF images were also collected at SSRL at beamline 2–3 using a Si(1 1 1) double crystal monochromator. The fluorescence signal was monitored with a Vortex Silicon Drift Detector. Samples were monitored at room temperature in air. In this experiment, the weathering profile maps were collected at 13000 eV and 5 × 5 μm pixel size for Se. Iron chemical maps were carried out with a 10 × 10 μm pixel size at six different energies (7114.9, 7121, 7126.2, 7126.4, 7137.1 and 7210 eV). An approximate distribution map for Fe(II) was generated in the SMAK software (Webb, 2011) by subtracting the background intensity at 7114.9 eV from the intensity at 7126.2 eV, which is dominated by Fe(II) in various minerals. An approximate distribution map for Fe(III) was generated by subtracting the Fe(II) distribution from total Fe (map at 7210 eV). Elemental profiles for Mn, Fe, Ca and K were obtained from the map collected at 7210 eV (~100 eV above the Fe K-edge). Due to limited beamtime, a map right above the Mn K-edge and below the Fe K-edge was not recorded, therefore the Mn map can still have residual signal from Fe because of high Fe content. The elemental profile for Zn was obtained from a map collected at 10 keV in the same region.

Iron K-edge μXANES spectra collected at SSRL were recalibrated according to the ALS XFM10.3.2 convention, using an Fe foil with first inflection point set at 7110.75 eV (Kraft et al., 1996). The spectra were analyzed with Athena software, IFFEFIT package 0.9.26 (Ravel and Newville, 2005). Least-squares linear combination fitting (LCF) of Fe K-edge μXANES data was subsequently performed using custom LabVIEW 2018 software available at beamline 10.3.2, following the procedures described elsewhere (Heller et al., 2017). LCF fits were performed in the range 7090 to 7365 eV, using the large Fe XAS database of XFM beamline 10.3.2 to confirm the oxidation state of Fe and further identify the major mineral groups present. The best fit, using a maximum of three components, was chosen based on the minimum normalized sum-square value ($NSS = 100 \times [\sum(\mu_{exp} - \mu_{fit})^2/\sum(\mu_{exp})^2]$), for which the addition of a spectral component to the fit required a 10% or greater improvement in the NSS value.

2.4. Rock magnetic analyses

Rock magnetic experiments were performed to detect and characterize ferromagnetic minerals, a term used broadly (in latin, *sensu lato*) to encompass minerals that have high magnetic susceptibility and can retain a remanent magnetization, but have a broad range of magnetic ordering behavior. The analyses were performed on bulk samples as well as samples of thin rock layers from three weathering profiles.

At the Institute for Rock Magnetism at the University of Minnesota, hysteresis loops and direct current (DC) demagnetization measurements were performed at room temperature using a Princeton Measurements Vibrating Sample Magnetometer (VSM). Seven samples (four from the weathering profile and three below it) were also subject to low-temperature experiments to further constrain the identification of ferromagnetic minerals. Using a Quantum Designs Magnetic Property Measurement System, samples were: (1) cooled in a 2.5 Tesla (T) field from 300 to 10 K, then the field was turned off, and remanence measurements were made upon warming (field-cooled low-temperature saturation isothermal remanent magnetization, FC LTSIRM); (2) cooled again to

10 K with no applied field, at 10 K pulsed with a 2.5 T field, and then remanence measurements were made upon warming (zero-field-cooled low-temperature saturation isothermal remanent magnetization, ZFC LTSIRM); (3) pulsed with a 2.5 T field at 300 K before cooling to 10 K and warming back to 300 K during which remanence measurements were collected (room temperature saturation isothermal remanent magnetization, RTSIRM).

These low-temperature experiments probe different aspects of temperature-dependent magnetic behavior. Sharp drops or increases in magnetization during warming and cooling cycles are related to well-characterized magnetic and/or crystallographic phase transformations of ferromagnetic minerals. RTSIRM curves can capture these transitions and their reversibility (or lack thereof) which gives insights into mineralogy and grain size. In addition to probing for these characteristic transitions, LTSIRM experiments compare warming curves where a sample was cooled under a strong field (FC) or not (ZFC) and can be used to identify additional minerals as some ferromagnetic minerals will differentially acquire magnetization under these conditions.

All samples were additionally analyzed at the UC Berkeley paleomagnetism lab using a 2G Enterprises superconducting rock magnetometer (SRM) with RAPID automatic sample handling and software (Kirschvink et al., 2008). Isothermal remanent magnetization (IRM) acquisition and alternating field demagnetization experiments were conducted to develop coercivity spectra with lower noise than on the VSM. Coercivity is an inherent property of ferromagnetic minerals related to how easily they are demagnetized (e.g., Peter and Dekkers, 2003), and coercivity spectra of specimens with complex mineral assemblages can be used to identify different mineral phases through peak fitting software; MaxUnMix was utilized here (Maxbauer et al., 2016). Several of the samples including those from the main fracture were additionally analyzed for rotational remanent magnetization (RRM) acquisition and demagnetization and anhysteretic remanent magnetization acquisition and demagnetization (before higher-field analyses at the University of Minnesota); data were processed using the RAPID Matlab codes (Kirschvink et al., 2008). The presence of RRM can be used to identify magnetic Fe-sulfide phases like pyrrhotite, although the sensitivity limits are not well understood (Thomson, 1990; Snowball, 1997).

3. Results

3.1. Bulk Measurements of Core Lithology and Weathering

The Redwell Basin core MW1, shown in Figs. 2a and S2, displays a hydrothermally altered and locally fractured sedimentary sequence composed of competent fine-grained sandstone interstratified with shale and siltstone (Thomas and Galey, 1982) (Fig. S3). Hydrothermal alteration led to the formation of polymetallic veins up to ~3-cm thick composed of quartz and sulfide minerals, increasing the heterogeneity of the sedimentary mineral association.

The topmost section of the core, from 2 to 2.8 m bgs, is unconsolidated and visibly weathered, with an ochre color. The depth of 2.8 m bgs marks an abrupt transition to more competent sandstone that contains varying fracture density and orientation with depth. Between 2.8 and 10.7 m bgs, a number of the fractures (approximately 10 out of 40) show evidence of weathering on the fracture surfaces. Beneath this depth, the fracture surfaces are unweathered. Manning et al. (2020) reported mineralogical, geological and groundwater geochemical data from the same core and borehole, MW1. The Mesaverde Formation at this location displays subhorizontal bedding-plane parallel fractures, and steeply dipping fractures (Fig. S3). The permeability is dominantly controlled by subhorizontal fractures, and currently active groundwater flow occurs close to the water table, the top of which fluctuates from approximately 8.8 m bgs down to a depth of 20 m bgs. Groundwater has an average pH of 5.5 at the water table position, increasing to 7.5 at the bottom of the drill hole (Manning et al., 2020).

3.1.1. X-ray Diffraction and Elemental Composition

Bulk rock XRD and XRD analyses of clay mineral separates reveal variations in mineralogy throughout the core (Fig. 2a). The uppermost weathered sample (2 m bgs) is dominated by quartz

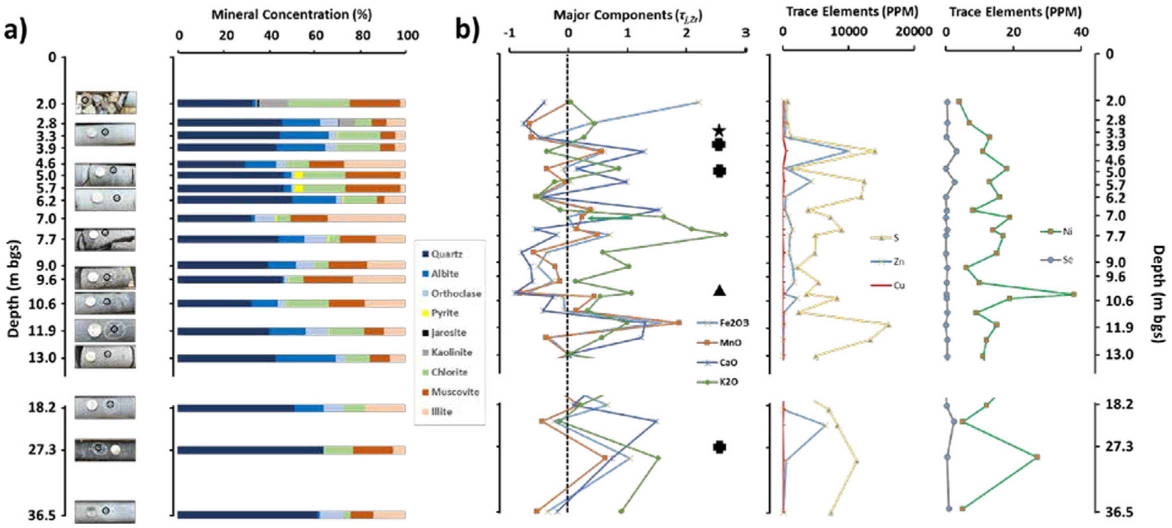

Fig. 2. Photographs and bulk mineral and elemental analyses of the Redwell Basin core MW1. (a) Bulk mineralogy of the MW1 core from bulk X-ray diffraction with photographs of select sample locations at selected depth. The coin shown is 1 inch in diameter. Rocks sampled at each depth can be seen in more detail in Fig. S2. Black circles with central "X" marks indicate the sampled location. (b) Bulk analysis of major and trace element concentrations, normalized using the mass transfer coefficient, τ_{Z_r}, with Zr as immobile element and using a white sandstone sample collected at 12.1 m bgs as the least altered reference sample. Star symbol marks the depth at which a fracture-surface sample was analyzed using room- and low-temperature magnetic methods and microscale X-ray fluorescence spectromicroscopy. Circle symbols mark depths at which background samples were analyzed by with room- and low-temperature magnetic methods. Triangle symbol marks depths at which additional fracture-surface samples were only analyzed with room-temperature magnetic methods. No symbols are included for the additional samples that were only analyzed magnetically at room-temperature.

(35%) and phyllosilicate minerals (62%) that bulk and clay mineral analyses identify as chlorite, illite, muscovite and kaolinite (Fig. S4), with complete loss of plagioclase and orthoclase. Below this position, the core is composed of 40 to 60% of quartz, 10 to 25% feldspar (mostly albite and orthoclase), and 10 to 40% chlorite and micas (illite and muscovite). The clay mineral and mica fractions reach 60% in some shale levels. Clay mineral analyses also identify vermiculite in the samples located above 5 m bgs (Fig. S4), the bulk XRD data cannot quantify its abundance. Accessory jarosite is detected by XRD only in one sample at 2 m bgs, whereas pyrite is detected at several depths (e.g., 3.3, 5.7 and 11.9 m bgs). However, paired SEM-EDX observations and magnetic analyses (detailed below) identify additional accessory minerals including pyrrhotite, magnetite, sphalerite, galena, several metal-oxides, calcite, and siderite.

Whole rock geochemistry shows depletion of S, Ca, and Zn above 3.3 m bgs with concomitant enrichment of Fe (Fig. 2b, Table S1 and S2). Below this, the S concentration displays strong variations with depth where samples that are enriched in S are also enriched in Zn, Ni, Mn, and/or Fe, especially at 3.9, 5.7, and 11.9 m bgs (Fig. 2b). Major elements such as Ca and K show highly variable concentrations, and their enrichments do not necessarily coincide with S and metal enrichments. Selenium has low concentrations throughout the core, but samples with relative Se enrichments are also relatively enriched in S. Finally, the C concentrations (Table S1) indicate that upper areas (above 3 m bgs) highly affected by weathering reactions contain much lower concentrations of carbonate minerals whereas less weathered samples display a variable concentration in carbonate minerals.

3.1.2. Rock Magnetic Analyses

Additional insights into Fe and S mineralogy in selected samples were obtained using non-destructive bulk magnetic techniques. These methods are very sensitive to ferromagnetic minerals, such as pyrrhotite, magnetite and siderite, but cannot detect non-ferromagnetic minerals such as pyrite or sphalerite. As a consequence, magnetic measurements do not provide complete mineralogical phase analysis. Nonetheless, most ferromagnetic minerals are reactive during weathering and thus may provide a proxy for weathering intensity even where present in low abundance.

3.1.2.1. Low-Temperature Magnetic Measurements. Low-temperature magnetic techniques reveal complex assemblages of ferromagnetic minerals (Fig. 3). Hematite and magnetite are identified in the samples based on their characteristic low-temperature magnetic transitions: the Morin transition at ~250 °K (hematite) and the Verwey transition at 120 °K (magnetite) (Verwey, 1939; Morin, 1950). Some of the magnetite may be partially oxidized to maghemite, even in unweathered samples, based on the slight humped shape of the RTSIRM curves (Ozdemir and Dunlop, 2010). Monoclinic pyrrhotite is identified by the non-reversible Besnus transition at 32 °K (Besnus and Meyer, 1964; Rochette et al., 1990) in all but one of the unweathered sandstone samples. Siderite becomes antiferromagnetic at low temperatures and can be identified in magnetic experiments due to its reversible magnetic transition at its Néel temperature of 37 °K and characteristic behavior of the FC LTSIRM values being much greater than those in the ZFC LTSIRM experiment (Frederich et al., 2003). Siderite is detected in all but the deepest of the unweathered samples. Due to similar transition temperatures, siderite identification is tentative in samples that contain both pyrrhotite and siderite and relied on qualitative comparison of the FC and ZFC LTSIRM experimental data.

3.1.2.2. Room-Temperature Magnetic Measurements. Room-temperature measurements of coercivity spectra can provide additional information on the ferromagnetic mineral content of a larger

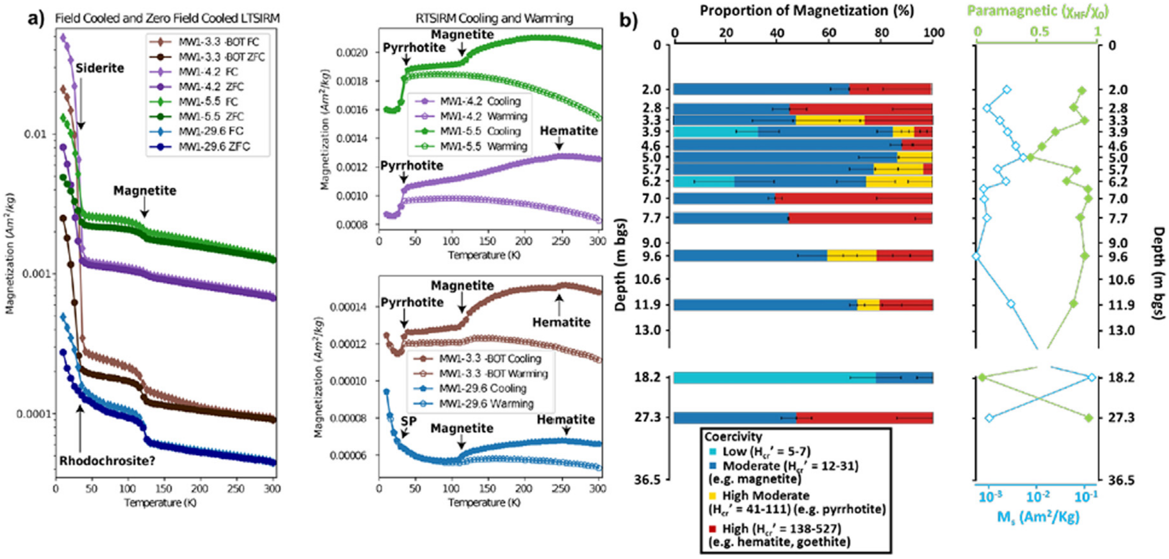

Fig. 3. Magnetic analysis of ferromagnetic minerals (*sensu lato*) in samples from the MW1 drill core (a) Low-temperature magnetic experiments from unweathered samples in the MW1 drill core at depths of 3.3, 3.9, 5.1 and 27.3 m bgs. Sample denoted 3.3-BOT is a ~2-mm thick rock slice from unweathered region of the fracture surface at 3.3 m bgs. Abbreviations: LTSIRM = low-temperature saturation isothermal remanent magnetization, FC = field cooled, ZFC = zero-field cooled, RTSIRM = room-temperature saturation isothermal remanent magnetization, SP = superparamagnetic minerals. (b) Relative proportions of magnetic mineral components in samples from the MW1 drill core based on fitting of IRM demagnetization coercivity spectra (Fig. S5). Ranges of coercivity values are consistent with minerals shown to be present through low-temperature magnetic methods. High coercivity (range of 139 to 527 mT, red) could be attributed to hematite and/or goethite; high-moderate coercivity (range 41 to 111 mT, yellow) is attributed to pyrrhotite; and moderate coercivity (range 12 to 31 mT, blue) is attributed to magnetite. The low coercivity component (range 5 to 7 mT, cyan) could be magnetite of a distinct grain size, titanomagnetite, unknown sulfide mineral, or coarse ferrihydrite. In the right plot, the saturation magnetism (M_s) in blue and the fraction of paramagnetic minerals in green (ratio of high-field to low-field susceptibility) obtained from hysteresis loops are shown. (For interpretation of the references to color in this figure legend, the reader is referred to the web version of this article.)

number of samples (Fig. 3b). The DC demagnetization data are noisy, due to the small sample-size and low abundance of ferromagnetic phases, such that interpretation of the IRM demagnetization data is aided by the more sensitive SRM data (even though the applied field values are lower) (Fig. S5). Due to overlapping coercivity ranges for different minerals (Peter and Dekkers, 2003), unique mineral identification even in numerically unmixed spectra is difficult. Nevertheless, with reference to the low-temperature experimental results, a moderate coercivity component (12 to 31 mT range from unmixed sample spectra) is tentatively linked with magnetite, a high-moderate coercivity (41 to 111 mT) is interpreted as pyrrhotite, and a high coercivity component (139 to 527 mT) is suggested to be hematite and/or goethite. A low coercivity component (5 to 7 mT) is difficult to interpret; it could be magnetite of a distinct grainsize (very-fine or very coarse) (Dunlop, 1986; Egli, 2004), titanomagnetite, a poorly characterized compositionally mixed sulfide minerals (Kim et al., 2000; Slotznick et al., 2019), or even very coarse ferrihydrite (Pannalal et al., 2005; Berquo et al., 2007).

The saturation magnetization at room temperature varies by over a factor of 100 across the 15 unweathered samples (note the log-scales in Fig. 3a and right plot in Fig. 3b). Saturation magnetization roughly correlates to the abundance of ferromagnetic minerals (especially pyrrhotite and magnetite) highlighting differences in the original unweathered bedrock.

The dominant feature in the sample coercivity data is an interval from ~3.7 to 6.7 m bgs that is enriched in ferromagnetic minerals inferred to be magnetite and pyrrhotite; these samples also show moderately high saturation magnetization values (Fig. 3b). This depth range includes one of the samples with detectable pyrite in XRD and an enrichment of Zn that reflects sphalerite in quartz veins, and thus represents a zone of higher hydrothermal fluid flow and mineralization associated with the porphyry intrusion. The uppermost two samples (2 m and 2.6 m bgs) contain only goethite/hematite and the moderate-coercivity component. One sample at ~18.3 m bgs exhibits more than an order of magnitude increase in magnetization as well as the largest proportion low-coercivity component and the lowest paramagnetic to ferromagnetic ratio.

3.2. Microchemical Analyses of Fracture-Scale Weathering

To elucidate the weathering processes distinct from the stratigraphic variations of hydrothermal alteration intensity, samples were prepared from a visibly weathered fracture surface at a depth of 3.3 m bgs (Fig. 4a). Sections cut normal to the fracture surface show evidence of weathering reactions, with an ochreous coating on mineral grains proceeding into the rock from the fracture surface (Fig. 4b and S6). The clay mineral content of the topmost layer, noticeable as fine-grained minerals in optical microscopy (Fig. S6), indicate that the fracture opened in a shale layer within the sandstone.

3.2.1. SEM-EDX Analysis

Two-dimensional imaging and elemental analysis using SEM–EDX on a polished thin section from the drill core shown in Fig. 4 confirmed the major mineralogy of the unweathered rock away from the fracture: dominantly quartz, plagioclase, orthoclase and chlorite. The SEM-EDX data show evidence of plagioclase and orthoclase replacement by sericite, which is fine-grained white mica that is a common and abundant hydrothermal alteration mineral in the phyllic and propylitic alteration zones of magmatic-hydrothermal ore deposits (Fig. 4c-III; Seedorff et al., 2005; Thomas and Galey, 1982). The SEM and XRD also identify Fe-rich chlorite and kaolinite (Fig. 4c-VII, S7 and S8). SEM analysis of the least weathered part of this sample documents the presence of accessory minerals such as sphalerite that may contain up to 10% Fe, minor galena that occurs locally as inclusions in sphalerite (Fig. 4c-V), and rare very fine-grained pyrrhotite that is identified by the Fe-S ratio in EDX analyses (Fig. 4c-IV and Fig. S8). Further-

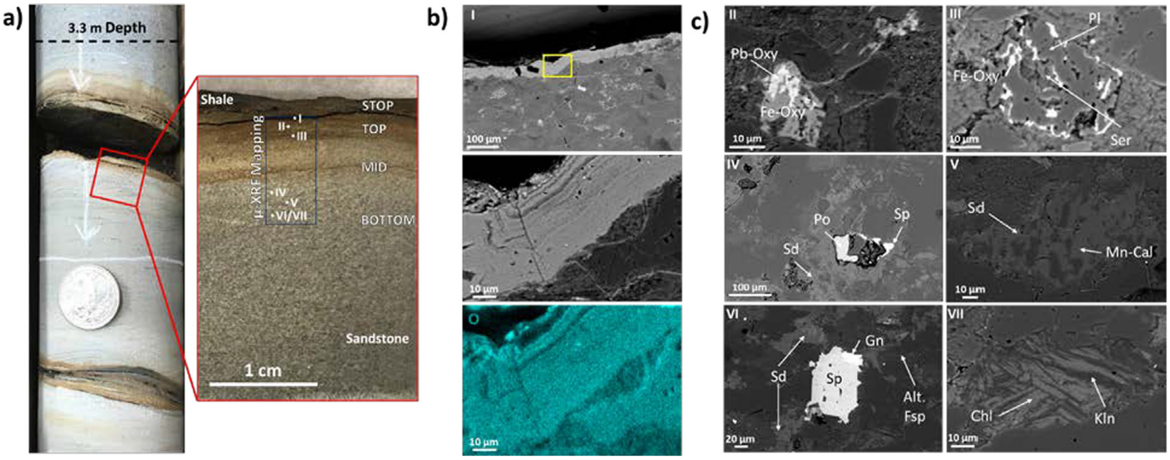

Fig. 4. (a) Photograph of the Mesaverde Formation drill core MW1 at a depth of 3.3 m bgs (left) and a cross-section of the core at the weathered fracture surface (right). The labels STOP, TOP, MID and BOTTOM refer to rock-chip samples cut from the same block for magnetism measurements. The purple square in the weathering profile indicates the area of µXRF mapping. The location of displayed SEM images are shown with white dots and are ordered according to their position with respect to the fracture surface, from the shallowest (I) to the deepest (VII). (b) The Fe-rich coating at the fracture surface where the layered banding is observed. (b-I) Back-scattered electron (BSE) image. (b-II) Higher-magnification BSE image from yellow box in b-I. (b-III) O distribution map. (c) BSE images from selected areas. (c-II) Intermixed lead and iron (oxyhydr)oxides (Pb- and Fe-Oxy) in the weathering region inferred to be the product of in-situ oxidation of metal sulfide minerals. (c-III) Plagioclase (Pl) grain, close to the fracture surface with irregular morphology consistent with hydrothermal alteration, associated with sericite (Ser) and iron (oxyhydr)oxide precipitation. (c-IV) Unweathered region showing evidence of pyrrhotite (Po) and sphalerite (Sp) co-precipitation with siderite (Sd) during hydrothermal alteration. (c-V) Intermixed siderite and Mn-rich calcite (Mn-Cal) in the unweathered region. (c-VI) Siderite, sphalerite and galena (Gn) precipitated from hydrothermal fluids in the unweathered region. Feldspar (Fsp) grains in the same region display pervasive hydrothermal alteration. (c-VII) Chlorite (Chl) from hydrothermal fluids in the unweathered region and kaolinite (Kln). Black areas in BSE images b-I, c-II, and c-III correspond to empty space (pores), which are not observed in other sample locations. Mineral identification is based upon energy-dispersive X-ray spectroscopy (EDX) data. Multi-element EDX maps from BSE images in b) and c) are shown in Figs. S7 and S8. (For interpretation of the references to color in this figure legend, the reader is referred to the web version of this article.)

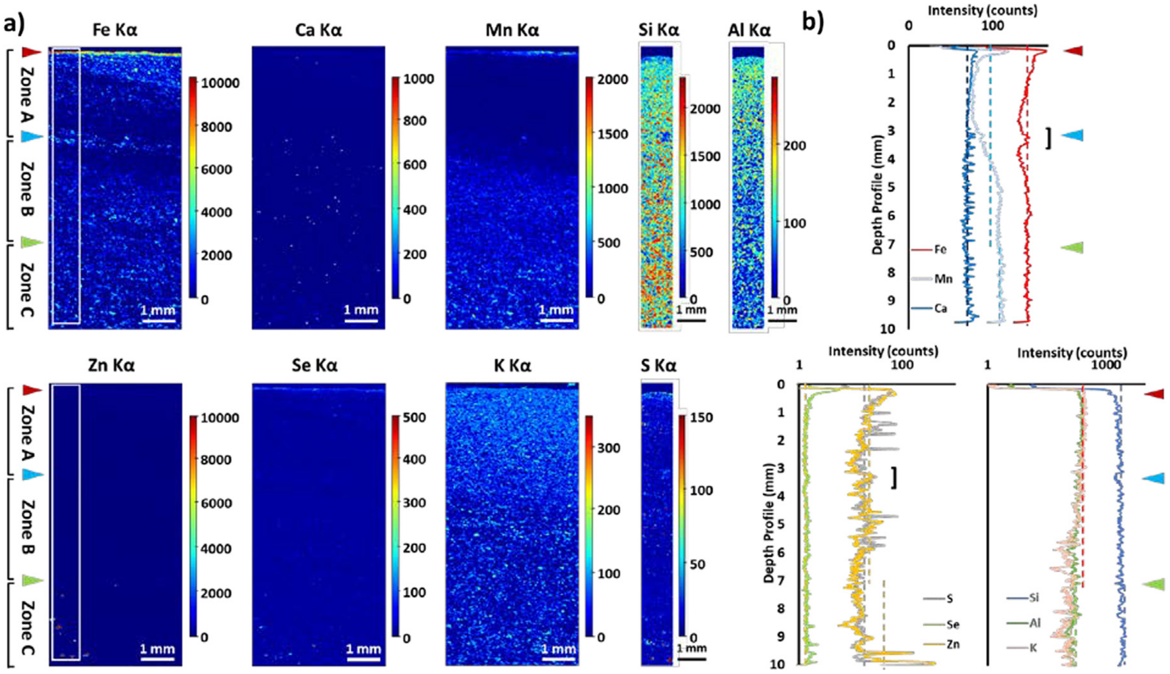

Fig. 5. Synchrotron µXRF maps (a) and integrated elemental profiles (b) of major and trace elements in the fracture weathering profile from MW1 core at 3.3 m bgs. The data reveal weathering profiles in Ca and Mn (top) and S, Zn and other elements (bottom). The red triangle indicates the fracture surface location, the blue triangle indicates the carbonate minerals and chlorite weathering front and green triangle indicates the sulfide minerals weathering front. Se map was recorded at 13000 eV (above the Se K-edge). The Zn map was collected at 10000 eV (above the Zn K-edge). The Fe, Mn, Ca, K maps were recorded at 7210 eV (above the Fe K-edge). These maps were recorded at SSRL 2–3. White rectangles indicate the Fe chemical mapping region. The Si, Al and S maps were recorded at 2522 eV (above the S K-edge) at ALS XFM 10.3.2. The elemental profiles are the horizontal integrations of the two-dimensional maps. The vertical dashed lines indicate the elemental average concentration above or below the oxidative weathering front (green arrows) for Fe, Mn, Ca, Si, Al, K, S, Se and Zn. The] symbol highlights the ~0.5-mm band of elevated iron and other elements inferred to represent weathering at a microfracture open to groundwater. (For interpretation of the references to color in this figure legend, the reader is referred to the web version of this article.)

more, Mn- and Fe-rich carbonate minerals are also observed in several areas (Fig. 4c-IV to VI, Fig S7 and S8). Pyrite is not observed.

Associated with the fracture surface, there is a ~1-cm thick weathering profile that is detectable by the absence of sulfide minerals, carbonate minerals and chlorite, and the presence of different accessory minerals. In unweathered rock, Mn is predominantly hosted in carbonate minerals with additional incorporation in chlorite, whereas in weathered areas Mn is absent and Fe oxides, Fe-oxyhydroxides and/or Fe-(oxyhydr)oxide-sulfates (from now on Fe-oxide) are pervasive and form pseudomorphs of the replaced minerals (i.e., sulfide minerals, Fig. 4c-II and S7).

In addition, a layer of Fe-oxides approximately 30-µm thick covers the fracture surface (Fig. 4b and S7). This coating is virtually pure Fe-oxide, with a final Mn oxides coat formed over the Fe precipitates, but lacking quartz or clay minerals. The expected Fe- and Mn-mineral phases are goethite and pyrolusite, respectively, which would be in equilibrium at the groundwater conditions (Bladh, 1982; Post, 1999; Manning et al., 2020). The coating exhibits interior banding in the BSE image concomitant with variations in O intensity, but not in the Fe or Mn elemental maps (Fig. 4b and S7).

3.2.2. µXRF and µXANES Analysis

Elemental distribution maps, integrated profiles of major and trace elements (Fig. 5), and trends in the oxidation states of iron (Fig. 6a) reveal a weathering profile with two distinct weathering fronts (located at ~3 and ~7 mm from the fracture surface) that divide the profile into three zones (A, B and C) characterized by different compositions. Zone C is the deepest and the least weathered area of the profile where sphalerite is confirmed by S K-edge µXANES and EDX (Fig. S8 and S9); the sphalerite also contains Se and Fe (Fig. 5). Iron K-edge µXANES from two locations in Zone C (spot 10 and 11, both ~8.5 mm from the fracture surface, Fig. 6 and S9) do not match any single reference, however LCF reveals the presence of Fe(II)-chlorite and siderite (Fig. 6 and S9), in agreement with XRD and EDX observations. The weathering front, at a distance of ~7 mm from the surface and highlighted by a green triangle in Fig. 5a, demarcates the unweathered region that contains discrete particles of sphalerite and the weathered area where sphalerite is absent. This weathering profile thus represents the front in the oxidative weathering of sulfide minerals and marks the division between weathered (Zones A and B) and unweathered rock (Zone C).

Zone B is a partially weathered area that lacks sphalerite, shows a gradient in Mn, and contains Ca-rich minerals that SEM-EDX data indicate are likely calcite. Zone A is the closest to the fracture, and most affected by weathering reactions that result in a loss of chlorite and sulfide minerals. The transition between Zones A and B occurs approximately 3 mm from the fracture surface and is shown by a blue triangle in Fig. 5a. It is defined by the calcite dissolution front inferred from the Ca distribution in µXRF mapping and SEM-EDX observations. Beneath this position, the Ca K-edge map (Fig. 5a) shows that Ca is concentrated in discrete areas (i.e., calcite grains). Above this position, calcite grains are absent, and Ca is distributed in a homogeneous background. Zone B shows a gradual loss of Mn towards the fracture surface (Fig. 5a) that is mirrored by a transition in Fe oxidation state from Fe(II) to Fe(III) (Fig. 6a). LCF of Fe K-edge µXANES from two locations (~4 and ~4.5 mm from the fracture surface) indicate the presence of chlorite (Muñoz et al., 2006) (Fig. 6 and S9), suggesting that this mineral is not affected by weathering in Zone B. Iron K-edge µXANES from different locations in the weathered region (Zones A and B) are consistent with goethite (Fig. 6, and S9). In addition, S K-edge XANES spectra and Fe suggest the presence of hydrous Fe-sulfate

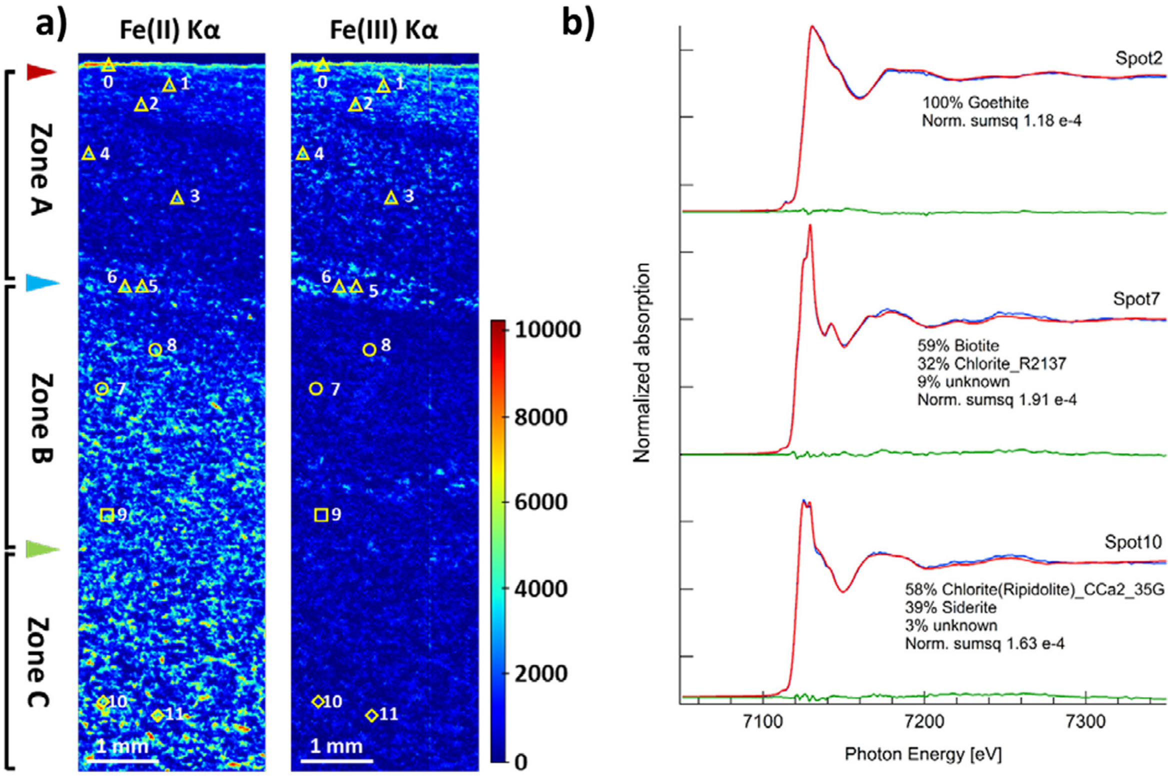

Fig. 6. (a) µXRF distribution maps of Fe(II) and Fe (III) in the fracture weathering profile from MW1 core at 3.3 m bgs were obtained by multi-energy mapping at SSRL beamline 2–3 (see methods section). Solid red triangle indicates the fracture surface location, the blue triangle indicates the carbonate minerals and chlorite weathering front and green triangle the sulfide minerals weathering front. Numbered locations indicated by the same geometric symbols (open triangle, circle, square or diamond) gave similar Fe K-edge µXANES spectra. (b) Fe K-edge µXANES spectra on representative spots along with best least-square linear combination fits (LCF), best matching goethite, chlorite, biotite and siderite. All spectra can be found in Fig. S9. (For interpretation of the references to color in this figure legend, the reader is referred to the web version of this article.)

minerals such as jarosite in Zone A and B (Fig. 7, S9) (Bigham and Nordstrom, 2000).

3.2.3. Rock Magnetic Analyses

Low-temperature rock magnetic experiments on samples from the four slices cut parallel to the weathered fracture surface at 3.3 m bgs (Fig. 3) reveal a large difference in the ferromagnetic mineral composition in the unweathered rock relative to the weathered rock close to the fracture (Fig. 8a). The slice that is furthest from the fracture surface (>10 mm) contains magnetite, pyrrhotite, and siderite. In contrast, the dark ochreous slice at the fracture is dominated by goethite, identified by a large progressive decrease in remanent magnetism during LTSIRM warming curves with higher remanence seen in FC LTSIRM experiments than ZFC LTSIRM experiments (Guyodo et al., 2003; Liu et al., 2006). The rate of decrease upon warming can change based on elemental impurities and grain size, with smaller grain sizes having a larger decrease (Dekker, 1989; Maher et al., 2004). The difference or spread between the FC and ZFC LTSRIM will also increase with decreasing grain size until grains become superparamagnetic in size (Guyodo et al., 2003, 2006; Lagroix and Guyodo, 2017). Based on these trends, we interpreted that at least some of the measured goethite at the fracture is sub-micron (nanophase) in size.

Rock slices contain an increasing amount of goethite as they get closer to the fracture surface, whereas pyrrhotite and magnetite decrease in abundance. Although pyrrhotite is not detectable in the RTSIRM and LTSIRM data from the fracture surface sample, as goethite dominate the low-temperature behavior and the Besnus transition is not visible (e.g., Swanson-Hysell et al., 2012), RRM measurements suggest pyrrhotite could be still present with $B_{eff} > \pm 20\ \mu T$ at 5 rps (Potter and Stephenson, 1986; Suzuki et al., 2006) (Fig. S10). Siderite is not found in all samples containing goethite.

Room temperature coercivity experiments on the same slices from the fracture surface at 3.3 m bgs also show trends with distance from the fracture and associated weathering intensity (Fig. 8b). The loss of the high-moderate coercivity contribution (attributed to pyrrhotite) is consistent with the profile in the oxidative weathering of sulfide minerals using SEM, µXRF and low-temperature magnetic methods. The presence of goethite associated with the loss of pyrrhotite cannot be easily probed with room-temperature rock magnetic data because the coercivity range for goethite is above the range probed using IRM demagnetization data. However, the sample closest to the fracture (STOP) shows a very-high-coercivity component using the noisier DC demagnetization curves corroborating insights from low-temperature analyses (Fig. S11) (Peter and Dekkers, 2003).

4. Discussion

The whole rock mineralogical and geochemical profiles in the 36-m Redwell Basin core display sharp variations that indicate a complex geological history where hydrothermal activity increased the heterogeneity of the original sedimentary rock. On the contrary, weathering-related mineralogical and geochemical transformations homogenized the affected rocks. Weathering occurs dominantly at fracture surfaces, indicating that groundwater flow through the relatively impermeable host rocks was fracture controlled. The integration of bulk rock analysis, X-ray, electron, and optical microscopy with magnetic measurements provide complementary support for key mineral reactions and products. We discuss the results from our study to propose a geochemical model for fracture-controlled and whole rock weathering, that we present below. In addition, although only present as trace mineral phases, the widespread distribution of pyrrhotite and siderite suggests a role for these reactive phases as indicators of the extent of rock weathering.

4.1. Bulk Hydrothermal Alteration and Weathering of Host Rock

The XRD and chemical analyses indicate that the most abundant minerals in the Mesaverde Formation are quartz, feldspar (albite and orthoclase) and chlorite, in agreement with previous descriptions (Gaskill et al., 1967) (Fig. 2). However, clay minerals are abundant, particularly illite and muscovite, whereas the feldspar concentration is lower in all samples with respect to standard value for the Mesaverde Formation. These clay minerals commonly occurred in marine sedimentary formations such as the underlying Mancos Shale and in hydrothermal alteration assemblages associated with porphyry deposits (Seedorff et al., 2005; Taylor and Macquaker, 2014). At Redwell Basin, magmatic hydrothermal processes altered sedimentary and diagenetic minerals, such as feldspar, into clay minerals as part of widespread propylitic and sericitic hydrothermal alteration related to porphyry Mo mineralization (Thomas and Galey, 1982). Pyrite also formed during hydrothermal activity, filling veins and forming common and widespread dissemination in the host rocks (Fig. S3).

Among the bulk samples of the MW1 drill core analyzed by all techniques, the samples at 2 and 27.3 m bgs exhibit the simplest bulk mineralogy and contain the lowest concentration of Zn, Cu and other metals (Figs. 2 and 3). In the case of sample at 27.3 m bgs, the observed chemical and mineralogical association suggest that it was the least hydrothermally altered and thus closest to parent rock. At this depth, feldspar minerals are not detected by XRD, probably as a consequence of particular sedimentary conditions given the low level of hydrothermal alteration. This sample also has the lowest overall remanent magnetism and contains magnetite and hematite. Magnetite is a common detrital mineral in sedimentary rocks (Maher, 2011) and can also form authigenically through clay mineral diagenesis (Lovley et al., 1987; Maher and Taylor, 1988; Kopp and Kirschvink, 2008; Kars et al., 2015). Due to its prevalence throughout the MW1 drill core, we posit that much of magnetite within this system was detrital or possibly early diagenetic and was preserved in low abundances (order of 0.001% wt). The exception is sample at 18.3 m bgs, where the strong magnetization suggests an increase in abundance of ferromagnetic phases, likely an increase in magnetite due to its strong saturation magnetization (Peter and Dekkers, 2003); we interpret that in this case the low-coercivity component is hydrothermal magnetite which formed in place of pyrrhotite during hydrothermal alteration (with the less likely possibility being a unique detrital composition during deposition).

The bulk rock data for the sample at 2 m bgs displays the effects of weathering. This sample is composed of unconsolidated, ochre-colored fragments, with the enrichment of goethite, the greatest concentration of clay minerals, and the depletion of sulfide minerals and feldspar. Hence, sulfide mineral weathering generated goethite, and silicate mineral weathering formed kaolinite, vermiculite and illite (Fig. 2a, 4b and S4). Ochre-colored fracture surfaces at other locations in the drill core reflect weathering at greater depth (e.g., at 7 and 10 m bgs). Due to the small rock volume affected, however, the consequences of weathering are not detectable by bulk elemental or mineralogical analyses, requiring the implementation of higher-spatial-resolution methods to determine weathering reaction pathways.

Magnetic measurements show that Fe(II) phases siderite or pyrrhotite are common in unweathered rock, although present at low concentration, but their absence from the sample at 27.3 m bgs suggests that these phases are not present in the sedimentary rock and are restricted to zones of hydrothermal alteration. Although modern examples of detrital pyrrhotite and early diagenetic pyrrhotite have been found in unique environments (Horng and Roberts, 2006; Larrasoana et al., 2007), most pyrrhotite forms directly in hydrothermal deposits, or as a result of low-temperature prograde metamorphism, where the loss of sulfur from pyrite formed pyrrhotite (Kissin and Scott, 1982; Hall, 1986; Craig and Vokes, 1993; Elmore et al., 2012). Siderite is absent in the deepest sample (Fig. 3a), but a magnetic signature interpreted to be rhodochrosite (Mn carbonate) is instead present (Frederich et al., 2003) as supported by SEM data. As discussed below, although only present as trace mineral phases, the widespread distribution of pyrrhotite and siderite suggests a role for these reactive phases as indicators of the extent of rock weathering.

4.2. Fracture-Scale Observations of Weathering

Microscale analysis of the fracture weathering profile at 3.3 m bgs by SEM, μXRF and μXANES (Figs. 4–7) provides information on mineral transformations and the redistribution and net loss or net gain of elements within the weathering profile. In Fig. 5, the average fluorescence emission counts (i.e., Fe, Mn, Ca, Si, Al and K) or median counts (i.e., S, Se and Zn) above and below the 7-mm (transition between Zone B and C) are plotted on top of the elemental profiles to assess whether mass balance is maintained during weathering. Fe and Ca show a similar average value above and below the second weathering front, even considering the high Fe accumulation at the fracture surface. Hence, Fe released during chlorite and Fe-bearing sphalerite dissolution, was transported towards the fracture surface but reprecipitated without loss to

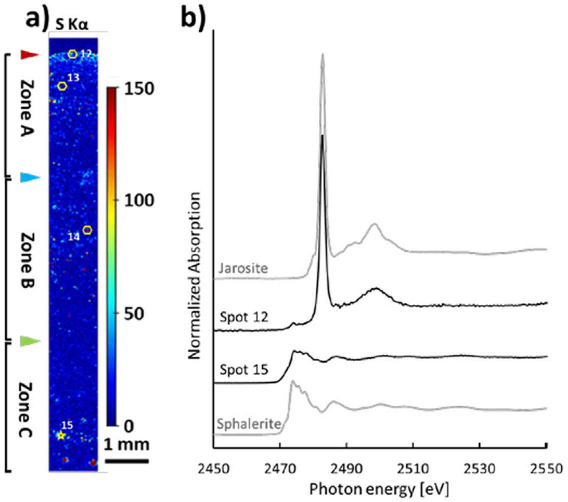

Fig. 7. (a) μXRF distribution maps of sulfur in the fracture weathering profile from MW1 core at 3.3 m bgs recorded at 2700 eV (above the S K-edge) from ALS beamline 10.3.2. The red triangle indicates the fracture surface location, the blue triangle indicates the carbonate minerals and chlorite weathering front, and the green triangle indicates the sulfide mineral weathering front. Numbered locations indicated by same geometric symbol (star and hexagon) gave similar S K-edge μXANES spectra. (b) Sulfur K-edge μXANES spectra obtained at selected numbered locations compared to bulk references from standards database. All spectra can be found in Fig. S9. (For interpretation of the references to color in this figure legend, the reader is referred to the web version of this article.)

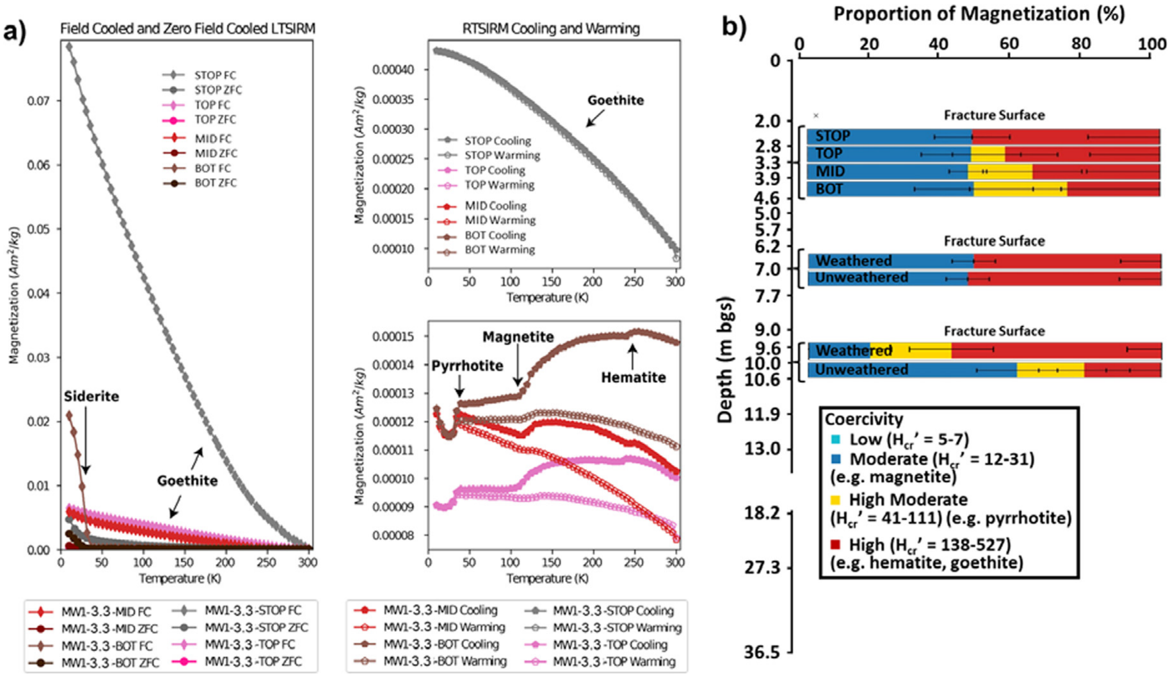

Fig. 8. Magnetic analysis of ferromagnetic minerals (*sensu lato*) in thin rock slices from three weathered fracture surfaces. (a) Low-temperature magnetic measurements on four rock slices cut from the weathered fracture surface at 3.3 m bgs. The slice locations are labeled in Fig. 4. BOT is the bottommost (unweathered, > 10 mm from the fracture surface) slice from the series and STOP is the fracture surface. The abbreviations of the measurement techniques are given in the Fig. 3 caption. (b) Relative proportions of magnetic mineral components based on fitting of IRM demagnetization coercivity spectra (Figs. S11 and S12). The interpretation of the ranges in coercivity values are given in the Fig. 3 caption.

groundwater. The conclusion that the Fe surface coating was generated from the rock and not deposited from groundwater is consistent with the groundwater pH (~7.5) because Fe-oxide phases are highly insoluble above pH 5. The banding of the coating could suggest that trace element chemistry controls the compositional banding but the low concentration of these elements prevents their detection by EDX. However, the weight and valence differences between trace elements with Fe and Mn would change the metal–oxygen ratio, explaining the bands observed in O map (Fig. 4b-I). The Fe-enriched layer at 3 to 3.5 mm, highlighted by square bracket symbol in Fig. 5b, is interpreted as a microfracture that served as a conduit for groundwater and additional localized weathering.

Two elements, Mn and Si display clear evidence of net loss to groundwater. Manganese is depleted from the fully weathered Zone A, although partially redeposited in the Fe-rich coating. According to SEM-EDX, Mn is mainly found as Mn-rich calcite; therefore, it makes sense that both Ca and Mn are found at the same depth, although Mn is more mobile than Ca. This front indicates the position in which carbonate minerals were totally dissolved, neutralizing the acidity generated by sulfide mineral dissolution, Fe(II) oxidation to Fe(III), and Fe-oxide precipitation. Silicon is depleted within ~300 μm at the fracture surface. Several elements, Zn, S, Se (Fig. 5) are enriched at the fracture surface. Zinc occurs at a greater concentration than in unweathered rock, indicating deposition from groundwater, likely through sorption to, or coprecipitation in, Fe(III) precipitates. The co-location of Se with Zn and S (Fig. 5) suggest that, in this sample, Se is dominantly hosted by sphalerite in the unweathered rock. but the mass balance for S, Zn and Se is difficult to assess due to the small numbers of particulate source minerals in the unweathered Zone C.

The weathering zone is enriched in Al and K, whose concentrations increase toward the fracture surface, suggesting that fine-grained mica is formed as a product of feldspar weathering, which is also consistent with Si depletion, following the equation:

$$NaAlSi_3O_8 + K^+ + 2H^+ + 2H_2O \Rightarrow KAl_3Si_3O_{10}(OH)_2 + 3Na^+ + 6\,H_4SiO_4 \quad (2)$$

The consumption of protons in equation 2 indicates that silicate dissolution consumes acidity generated by sulfide minerals oxidation in a neutralization reaction. The presence of dissolution textures throughout the profile indicate that weathering reactions were superimposed over a complex hydrothermal alteration mineral assemblage. The observation of Fe-oxide mineral precipitates around feldspar grains with dissolution pits, found uniquely in Zones A and B (Fig. 4c-III), strongly indicates that feldspar dissolution neutralized acidity generated by Fe(II) oxidation to Fe(III) and Fe-oxide precipitation. Silicate dissolution is slower than carbonate mineral dissolution but likely contributes to acidity neutralization long after carbonate minerals are fully consumed.

Surprisingly, pyrite is not observed in optical, electron or X-ray analyses of any of our samples even though hand sample observations showed it to be the most abundant sulfide mineral in the MW1 core, and it is detected by XRD in many samples (Fig. 2a). Either pyrite was not formed in the rock at the analyzed locations, or it was preferentially oxidized in the weathering profile before other sulfide minerals such as sphalerite. In either case, pyrite oxidation is a potential source of remobilized Fe. Taken together, all analytical data suggest that the weathering reactions in Zones A and B involved the total or partial dissolution of sulfide minerals (i.e., pyrite, sphalerite and pyrrhotite), carbonate minerals (i.e., calcite, Mn-bearing calcite and siderite), as well as the acid-promoted total or partial dissolution of silicate minerals (i.e., chlorite and feldspar).

SEM imaging show that weathering reactions caused a net increase in rock pore volume with clear differences between locations close to the fracture surface (Fig. 4b-I to Fig. 4c-III) and those in the unweathered rock (Fig. 4c-IV to Fig. 4c-VII). Specially, the presence of void space between unweathered minerals at the fracture surface is clear, whereas the unweathered rock lacks these holes and spaces. This increasing porosity could be the consequence of (1) dissolution of reactive minerals such as carbonate minerals, or (2) volume change during mineral replacement reactions. Therefore, weathering increased the porosity in areas closer to the fracture, thereby enhancing the diffusion of reactive species in pore water toward the unweathered rock.

4.3. Cross-Scale Mineral Signatures of Weathering Extent

The weathering reactions described in detail at the weathering profile at 3.3 m bgs may be extrapolated to explain the observed mineral assemblage resulting from weathering at the drill core scale.

Magnetic analysis of rock slices at fracture scale revealed transitions in Fe mineralogy attributable to weathering (Fig. 8). The low-temperature data indicate that weathering caused a loss of magnetite, pyrrhotite, and siderite. The room-temperature coercivity measurements at this depth are consistent with the loss of magnetite and pyrrhotite. A shift in the moderate coercivity peak is noted from the unweathered to the weathered sandstone samples suggesting a preferential weathering of minerals with lower coercivity, potentially very large or very small magnetite grains (Dunlop, 1986; Egli, 2004) (Fig. S11). In addition, weathering was associated with the formation of goethite, at least some of which is nanometric, as evidenced in the low-temperature magnetic and Fe K-edge µXANES data (Fig. 6b). Siderite also weathered rapidly with a sharp transition noted between the unweathered and weathered rock (~10 mm from the fracture surface) above which siderite is not detected and goethite appears. These observations agree with the SEM-EDX results, displaying both pyrrhotite and siderite in the least weathered area only (Fig. 4c-IV to 4c-VII). These trends are partially repeated in the weathering profile at 10 m bgs, where a small decrease in the moderate coercivity component (magnetite) accompanies the complete loss of a high-moderate coercivity component (pyrrhotite). No pyrrhotite and weatherable magnetite are detected in the fracture at 7 m bgs, suggesting that this sample was more fully weathered than anticipated by visual inspection (Fig. 8 and S12). Therefore, magnetite, siderite and pyrrhotite can be included in the list of minerals affected by weathering, contributing to the total Fe that is initially remobilized by oxidation and subsequently retained by goethite precipitation.

Magnetic measurements at the meter-scale are consistent with fracture-scale results. Bulk samples below 2.6 m bgs display pyrrhotite and/or siderite except in those less affected by hydrothermal activity (i.e., 27.3 m bgs, Fig. 3), whereas the shallowest and the most weathered samples contain only goethite/hematite and the moderate-coercivity component. Therefore, the anticorrelation between ferromagnetic minerals, especially pyrrhotite, and goethite abundance could be used as a proxy to indicate weathering intensity in mineralized rocks at any scale. These observations also indicate that the mineralogical and chemical heterogeneity imposed by hydrothermal alteration were at least partially homogenized by weathering reactions as, for example, pyrite, pyrrhotite, siderite, and Fe(II)-chlorite weathering all led to the precipitation of Fe-oxide (mostly goethite).

Silicate minerals also showed analogous trends in fracture- and core-scale data. The depletion of feldspar and chlorite, and the increase in illite and muscovite observed in shallower samples at drill core MW1 (Fig. 2) reflects the replacement of feldspar with sericite observed in the fracture weathering profiles at 3.3 m bgs (Fig. 4c-III) as described by reaction (2). The high clay mineral and low feldspar concentrations throughout the drill core could be interpreted as the effect of hydrothermal alteration (Fig. 2). Both hydrothermal and acidic conditions could cause the dissolution textures observed in feldspar at the microscale (Fig. 4c-III). However, the increasing clay mineral content toward the surface (both the fracture surface and the top of the drill core) shows the contribution of weathering to reaction (2).

The S content and carbonate mineral estimation indicate that only bulk core samples above 2.6 m bgs lack sulfides and carbonates (Fig. 2 and Table S1). Similar trends are observed by SEM-EDX and µXRF mapping, where the less weathered regions at fracture scale (Zone C) display both carbonate and sulfide minerals, which gradually disappear toward Zone A (Figs. 4–7). The fracture-scale data additionally show that pyrite oxidation precedes carbonate dissolution and hence indicate that carbonate dissolution neutralizes acidity generated by sulfide oxidation.

The behavior of trace elements such as Se is more difficult to compare between scales. Selenium was released from sulfide minerals and, at the fracture scale, it was redistributed but overall retained within the weathered region, likely through sorption or co-precipitation (Peak and Sparks, 2002; Sherman and Randall, 2003). The ability of Fe-oxides to retain trace elements at sites impacted by sulfidic rock weathering is well-documented (e.g., Gunsinger et al., 2006; Holmstrom and Ohlander, 2001) (Fig. 5b). However, the Fe accumulation above 2.6 m bgs at drill core MW1 is not correlated with elevated Se concentration, which is in contrast totally depleted. Similar discrepancies are observed for Zn. Some differences in weathering pathways between locations and across scales are expected, for example, the influence of organic reaction near the ground surface (Hasenmueller et al., 2017; Hubbard et al., 2018).

In summary, most of the mineral reactions and element trends associated with weathering can be identified at both the core and fracture scales. Samples nearest the top of MW1 drill core (i.e., 2 and 2.6 m bgs) are highly weathered with similar mineral composition as Zone A at the fracture scale. Similarly, the partially-weathered drill core section displays weathering profiles around fractures (i.e., from 2.6 to 10 m bgs, Fig. 8) and could be correlated to Zone B at the fracture scale. Finally, the core section below 10 m bgs is least weathered and can be correlated with Zone C at the fracture scale. The development of a plausible geochemical model for weathering, however, is most accurately obtained through the analysis of fracture-scale data.

4.4. Conceptual Model

The results obtained in this research allow a geochemical model to be developed describing the principal mineral and elemental transformations and element mobility (Fig. 9). This model displays the general weathering reactions identified at both scales, and could be adapted to local variation in parameters such as mineralogical variation (e.g., absence of pyrite) and changes in the rock structure (e.g., fracture density). Iron was mostly released at MW1 by oxidation of pyrite, but also by the weathering of chlorite, Fe-rich sphalerite, siderite, pyrrhotite and magnetite (Figs. 2–8). Iron transport was accompanied by precipitation of jarosite (an Fe-oxyhydroxide sulfate, Figs. 2 and 7), and goethite (Figs. 3, 6 and 8). At the fracture scale, the presence of the stable mineral phase jarosite, which preferentially forms at pH values below 2.5 in the presence of Fe(III) and sulfate (Bigham et al., 1996), suggesting acidic pore water. At higher pH in pore water, the metastable phase schwertmannite forms more readily than jarosite, but recrystallizes over months to form goethite thereby liberating sulfate (Bigham et al., 1996; Acero et al., 2006). In such acidic pore water, both Fe^{+2} and Fe^{+3} species are mobile (Bigham and Nordstrom, 2000) and the detection of some Fe(II) in the surface

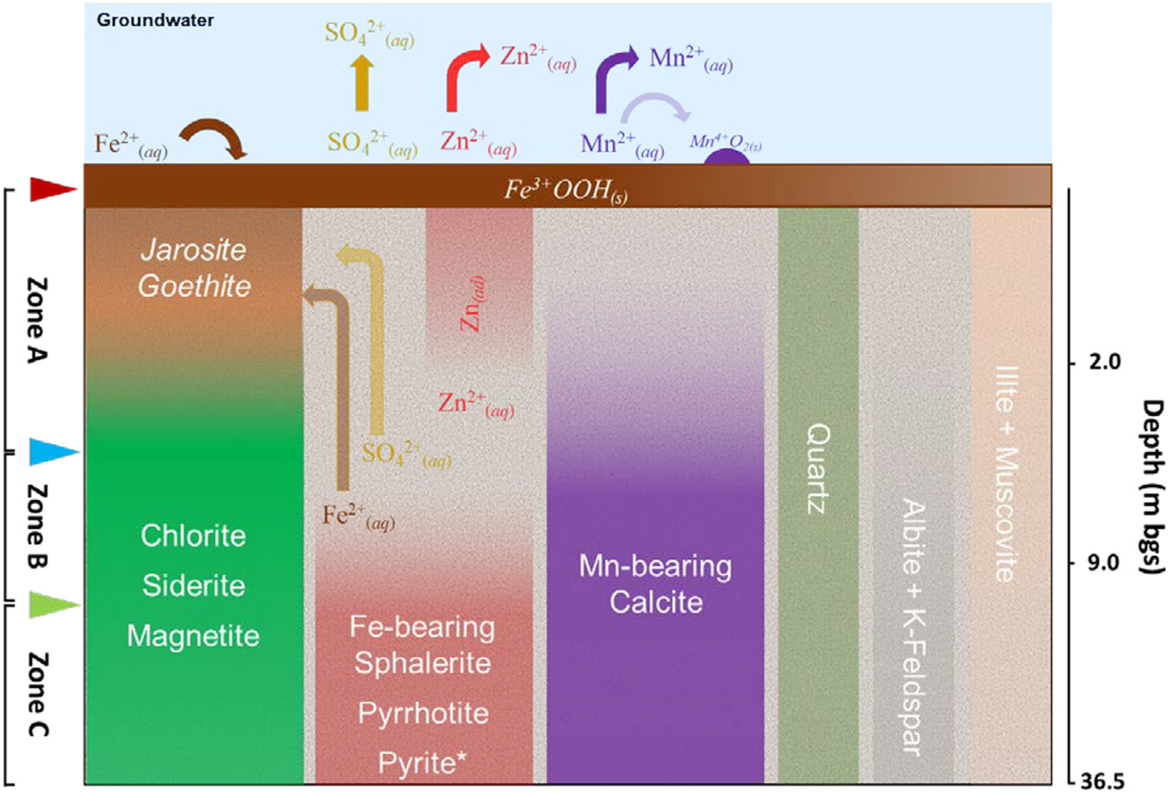

Fig. 9. Conceptual model of the fracture-scale weathering profile observed in mineralized Mesaverde Formation sandstone, showing the principal weathering fronts, element transport within the rock and retention or release into groundwater. Red triangle indicates the rock-groundwater interface at the fracture, the blue triangle indicates the chlorite and carbonate mineral weathering front, and the green triangle indicates the sulfide mineral weathering front. Minerals that dissolve (e.g., sphalerite) or that precipitate (e.g., jarosite) during weathering are written in normal and italic text, respectively. Zinc cations are partly retained, likely by adsorption to goethite. Quartz is distributed throughout the rock and is negligibly dissolved during weathering. Feldspar (Albite and K-Feldspar) and chlorite are partially dissolved during weathering, whereas muscovite and illite (i.e., sericite) increase their abundant toward the fracture surface. *Pyrite is included in the conceptual model as one of the main sources of Fe in this system, even though it was not detected at the 3.3 m MW1 weathering profile. Abbreviations: Zn(ad) = adsorbed zinc. (For interpretation of the references to color in this figure legend, the reader is referred to the web version of this article.)

coating is consistent with at least part of the Fe diffusing as Fe^{+2} to the fracture (Fig. 6). The sorption of soluble Fe(II) to goethite and solid-state electron transfer could provide a mechanism for long-term stabilization of Fe(II) (Williams and Scherer, 2004; Handler et al., 2009). The increasing Fe content towards the fracture and the coating of goethite along the fracture are consistent with the neutralization of acidic pore water as it mixes with the circumneutral groundwater at MW1 (Manning et al., 2020). Although a goethite coating could form by precipitation of Fe from oversaturated groundwater (Parviainen et al., 2015), the overall mass conservation of Fe strongly indicates that all the coating originated from local weathering reactions inside the rock (Fig. 5). These reactions may be extrapolated to the meter-scale, where the ochreous precipitates coating the host rock, the jarosite and goethite detection by XRD and magnetism, respectively, and the high Fe accumulation with respect to the parent rock at the top of the drill core indicate that Fe was retained after weathering of the host rock in MW1 (Figs. 2, 3 and S2).

The oxidation of pyrite and Fe-rich sphalerite were the two reactions that generated acidity (Moncur et al., 2009; Çelebi and Öncel, 2016), which was partially neutralized by the complete dissolution of carbonate minerals (calcite, Mn-bearing calcite and siderite) and the partial dissolution of reactive silicate minerals (feldspar and chlorite) remaining from prior hydrothermal alteration. The elevated relative abundances of K and Al near the fracture and the anticorrelation between feldspar and clay minerals content throughout the drill core are consistent with clay mineral formation resulting from acid-promoted feldspar and chlorite dissolution and subsequent clay mineral precipitation (kaolinite, illite, muscovite and vermiculite, Figs. 2, 5, 6 and 7). Sphalerite oxidation was also the source of Zn that, in contrast to Fe, was mostly lost from the weathered rock (Fig. 2b and 5). Secondary Zn phases could not be identified and only a diffuse distribution associated with Fe suggests that Zn was partially co-precipitated with, or adsorbed onto Fe(III)-phase products (Waychunas et al., 2005). Manganese was also mainly lost from the weathering rock and partially accumulated on top or within Fe coatings (Fig. 2b and 5). The sharp weathering profile observed at fracture scale is consistent with diffusion-limited dissolution of carbonate minerals, neutralizing pH in pore water (Fig. 5). The retention of some Mn-oxide as pyrolusite on the goethite fracture coating, which requires slightly acid to neutral pH (Post, 1999), supports the conclusion of a strong pH gradient between the pore water in the rock and the groundwater in the fracture. Because these pyrolusite precipitates are sparse, Mn mobility may be controlled by seasonal variations in pH and dissolved inorganic carbon (Sullivan et al., 2016; Hubbard et al., 2018). Seasonal variation might explain the layered texture of the surface coating evident in the SEM data if the Fe-phases were weathered following precipitation by changes in groundwater chemistry (Cruz-Hernández et al., 2019) (Fig. 4b). However, X-ray microprobe and magnetic measurements are dominated by goethite, so the banding could also be attributed to variation in density due to the content of trace elements (Figs. 7 and 8). Although pyrolusite is not detected in the shallowest samples in

MW1, Mn accumulation with respect to parent rock and circumneutral groundwater pH are also consistent with pyrolusite precipitation and/or sorption into Fe-oxides minerals.

5. Conclusions

The coupled geochemical, X-ray spectromicroscopy and rock magnetic data in this study support a conceptual model for the weathering of sulfidic sedimentary rocks that follows a common geochemical pattern. Specifically, the abundance of sulfide mineral controls the generation of acidity and dissolved elements, the abundance of neutralizing minerals determines the pore-fluid pH, and pH-dependent mobility of dissolved elements controls their transport to the groundwater. This model likely holds regardless of the source of the disseminated sulfide minerals (e.g., hydrothermal alteration or diagenesis) and the nature of the neutralizing mineral phases (i.e., carbonate minerals, chlorite, and feldspar).

This study concludes that weathering at the studied location and depth made little contribution to the export of acidity and metals, which is consistent with prior field and simulation studies in many regions of the Redwell Basin (Kimball et al., 2010). Therefore, the acid drainage that occurs in the Redwell Basin was not a consequence of weathering throughout the basin itself. It was likely the result of the weathering in highly mineralized areas, where the acidity generated by pyrite and Fe oxidation cannot be totally neutralized by carbonate and silicate minerals dissolution, as well as acid pore water dilution by mixing with circumneutral groundwater. The data presented here from the Redwell Basin should be compared with those from other areas where rocks with high pyrite concentrations are affected by weathering, to refine this conceptual model and application to other systems with different sulfide mineral content.

The conceptual model of Fig. 9 could also provide a basis for understanding past and future weathering processes throughout the sandstone sequences of the MW1 drill core, provided that variations in abundance of mineral phases abundance are considered. Predicting the potential metal exports from the rock as the active weathering front descends is challenging, because phases such as sphalerite, observed by synchrotron microfocused X-ray spectromicroscopy, were never detected using bulk XRD. However, magnetic data track the loss of the sulfide pyrrhotite and the formation of goethite in the well-studied fracture surface at 3.3 m bgs and at core scale. These paired magnetic measurements thus could offer a proxy for weathering extent in hydrothermally altered sulfidic rock.

Declaration of Competing Interest

The authors declare that they have no known competing financial interests or personal relationships that could have appeared to influence the work reported in this paper.

Acknowledgements

This work was conducted as part of the Watershed Function Scientific Focus Area at Lawrence Berkeley National Laboratory (LBNL) and was supported by the U.S. Department of Energy (DOE) Subsurface Biogeochemical Research Program, DOE Office of Science, Office of Biological and Environmental Research, under Contract Number DE-AC02-05CH11231. SC was partly supported by the NSF Geobiology and Low-Temperature Geochemistry program under Grant No. 1324791 and by IDAEA-CSIC as a Severo Ochoa Centre of Research Excellence (Spanish Ministry of Science and Innovation, Project CEX2018-000794-S). SPS was partially supported by a Miller Institute for Basic Research in Science Fellowship. Use of XFM beamline 10.3.2 at the Advanced Light Source at LBNL was supported by the DOE Office of Science, Office of Basic Energy Sciences under Contract No. DE-AC02-05CH11231. Use of beamline 2-3 at the Stanford Synchrotron Radiation Light Source, SLAC National Accelerator Laboratory, was supported by the DOE Office of Science, Office of Basic Energy Sciences under Contract No. DE-AC02-76SF00515. Many of the rock magnetic experiments were conducted during a visiting fellowship to BG at the Institute for Rock Magnetism which is supported by the National Science Foundation and the University of Minnesota. We thank Mike Jackson and Josh Feinberg for assistance and insight at the Institute for Rock Magnetism. We also thank Yiming Zhang for assistance with magnetic measurements at the UC Berkeley Paleomagnetism Lab (with support from NSF EAR-1925990) and Marco Voltolini for assistance with diffraction measurements in Berkeley. Any use of trade, firm, or product names is for descriptive purposes only and does not imply endorsement by the U.S. Government.

Appendix A. Supplementary material

(1) Geographic map of the Colorado River Basin, (2) Photographs of MW1 core boxes with indication of sample location, (3) The geological description of the core MW1, (4) XRD of clay mineral fractions, (5) Coercivity spectra from all unweathered samples from core MW1, (6) Details of the weathering profile location at 3.3 m depth in core MW1. (7) Elemental maps obtained with EDX at 3.3 m MW1 weathering profile, (8) Elemental composition of selected spots by EDX, (9) All Fe K-edge and S K-edge XANES spectra collected at 3.3 m bgs MW1 weathering profile, including corresponding best LCF of Fe K-edge fits, (10) Rotational remanent magnetization data, (11-12) Coercivity spectra of rock slices at weathering fracture surfaces from other depths in the MW1 core and (Tables S1 and S2) Major and trace elemental composition in core MW1. Supplementary material to this article can be found online at https://doi.org/10.1016/j.gca.2022.11.005.

References

Acero, P., Ayora, C., Torrentó, C., Nieto, J.M., 2006. The behavior of trace elements during schwertmannite precipitation and subsequent transformation into goethite and jarosite. Geochim. Cosmochim. Acta 70, 4130–4139.

Alford, L., Gysi, A.P., Hurtig, N.C., Monecke, T., Pfaff, K., 2020. Porphyry-related polymetallic Au-Ag vein deposit in the Central City district, Colorado: Mineral paragenesis and pyrite trace element chemistry. Ore Geol. Rev. 119, 103295.

Anderson, S.P., Dietrich, W.E., Brimhall, G.H., 2002. Weathering profiles, mass-balance analysis, and rates of solute loss: Linkages between weathering and erosion in a small, steep catchment. Bull. Geol. Soc. Am. 114, 1143–1158.

Bao, Z., Al, T., Bain, J., Shrimpton, H.K., Finfrock, Y.Z., Ptacek, C.J., Blowes, D.W., 2022. Sphalerite weathering and controls on Zn and Cd migration in mine waste rock: An integrated study from the molecular scale to the field scale. Geochim. Cosmochim. Acta 318, 1–18.

Berquo, T.S., Banerjee, S.K., Ford, R.G., Penn, R.L., Pichler, T., 2007. High crystallinity Si-ferrihydrite: An insight into its Néel temperature and size dependence of magnetic properties. J. Geophys. Res. 112, 1–12.

Besnus, M., Meyer, A., 1964. Nouvelles données expérimentales sur le magnétisme de la pyrrhotine naturelle. In Conference of Magnetism, Nottingham.

Bigham, J.M., Nordstrom, D.K., 2000. Iron and aluminum hydroxysulfates from acid sulfate waters. Rev. Mineral. Geochem. 40, 351–403.

Bigham, J.M., Schwertmann, U., Traina, S.J., Winland, R.L., Wolf, M., 1996. Schwertmannite and the chemical modeling of iron in acid sulfate waters. Geochim. Cosmochim. Acta 60, 2111–2121.

Bladh, K.W., 1982. The formation of goethite, jarosite, and alunite during the weathering of sulfide-bearing felsic rocks. Econ. Geol. 77, 176–184.

Blodau, C., 2006. A review of acidity generation and consumption in acidic coal mine lakes and their watersheds. Sci. Total Environ. 369, 307–332.

Bondu, R., Cloutier, V., Rosa, E., Benzaazoua, M., 2016. A review and evaluation of the impacts of climate change on geogenic arsenic in groundwater from fractured bedrock aquifers. Water. Air. Soil Pollut. 227, 296.

Brantley, S.L., Lebedeva, M., 2011. Learning to read the chemistry of regolith to understand the critical zone. Annu. Rev. Earth Planet. Sci. 39, 387–416.

Brimhall, G.H., Dietrich, W.E., 1987. Constitutive mass balance relations between chemical composition, volume, density, porosity, and strain in metasomatic hydrochemical systems: Results on weathering and pedogenesis. Geochim. Cosmochim. Acta 51, 567–587.

Buss, H.L., Sak, P.B., Webb, S.M., Brantley, S.L., 2008. Weathering of the Rio Blanco quartz diorite, Luquillo Mountains, Puerto Rico: Coupling oxidation, dissolution, and fracturing. Geochim. Cosmochim. Acta 72, 4488–4507.

Çelebi, E.E., Öncel, M.S., 2016. Determination of acid forming potential of massive sulfide minerals and the tailings situated in lead/zinc mining district of Balya (NW Turkey). J. African Earth Sci. 124, 487–496.

Chapin, C.E., 2012. Origin of the Colorado Mineral Belt. Geosphere 8, 28–43.

Chevrier, V., Mathé, P., Rochette, P., Gunnlaugsson, H.P., 2006. Magnetic study of an Antarctic weathering profile on basalt: Implications for recent weathering on Mars. Earth Planet. Sci. Lett. 244, 501–514.

Chung, F.H., 1974. Quantitative interpretation of X-ray diffraction patterns of mixtures. I. Matrix-flushing method for quantitative multicomponent analysis. J. Appl. Crystallogr. 7, 519–525.

Craig, J.R., Vokes, F.M., 1993. The metamorphism of pyrite and pyritic ores: an overview. Mineral. Mag. 57, 3–18.

Cruz-Hernández, P., Carrero, S., Pérez-López, R., Fernandez-Martinez, A., Lindsay, M. B.J., Dejoie, C., Nieto, J.M., 2019. Influence of As(V) on precipitation and transformation of schwertmannite in acid mine drainage-impacted waters. Eur. J. Mineral. 31, 237–245.

Dekker, M., 1989. Magnetic properties of natural goethite—II. TRM behaviour during thermal and alternating field demagnetization and low-temperature treatment. Geophys. J. Int. 97, 341–355.

Dessert, C., Dupré, B., Gaillardet, J., François, L.M., Allègre, C.J., 2003. Basalt weathering laws and the impact of basalt weathering on the global carbon cycle. Chem. Geol. 202, 257–273.

Dunlop, D.J., 1986. Hysteresis properties of magnetite and their dependence on particle size: A test of pseudo-single-domain remanence models. J. Geophys. Res. 91, 9569–9584.

Egli, R., 2004. Characterization of individual rock magnetic components by analysis of remanence curves, 1. Unmixing natural sediments. StGG 48, 391–446.

Elmore, R.D., Muxworthy, A.R., Aldana, M., 2012. Remagnetization and chemical alteration of sedimentary rocks. Geolofical. Soc. London Spec. Publ. 371, 1–21.

Essalhi, M., Sizaret, S., Barbanson, L., Chen, Y., Lagroix, F., Demory, F., Nieto, J.M., Sáez, R., Capitán, M.Á., 2011. A case study of the internal structures of gossans and weathering processes in the Iberian Pyrite Belt using magnetic fabrics and paleomagnetic dating. Miner. Depos. 46, 981–999.

Frederich, T., Von Dobeneck, T., Bleil, U., Dekkers, M., 2003. Towards the identification of siderite, rhodochrosite, and vivianite in sediments by their low-temperature magnetic properties. Phys. Chem. Earth, Parts A/B/C 28, 669–679.

Gaillardet, J., Dupré, B., Louvat, P., Allègre, C.J., 1999. Global silicate weathering and CO2 consumption rates deduced from the chemistry of large rivers. Chem. Geol. 159, 3–30.

Gaskill, D.L., Godwin, L.H., Mutschler, F.E., 1967. Geologic map of the Oh-be-Joyful quadrangle, Gunnison county, Colorado. U.S Geol. Surv. Map GQ-578.

Gaste-Rector, S.D., Blanton, T.N., 2019. The powder diffraction file: A quality materials characterization database. Powder Diffr. 34, 352–360.

Gray, N.F., 1998. Acid mine drainage composition and the implications for its impact on lotic systems. Water Res. 32, 2122–2134.

Gu, X., Heaney, P.J., Reis, F.D.A.A., Brantley, S.L., 2020. Deep abiotic weathering of pyrite. Science (80-.) 370.

Gunsinger, M.R., Ptacek, C.J., Blowes, S.W., Jambor, J.L., Moncur, M.C., 2006. Mechanisms controlling acid neutralization and metal mobility within a Ni-rich tailings impoundment. Appl. Geochem. 721, 1301–1321.

Guyodo, Y., Mostrom, A., Lee, P.R., Banerjee, S.K., 2003. From nanodots to nanorods: Oriented aggregation and magnetic evolution of nanocrystalline goethite. Geophys. Res. Lett. 30, 1512.

Guyodo, Y., Lapara, T.M., Anschutz, A.J., Penn, R.L., Banerjee, S.K., Geiss, C.E., Zanner, W., 2006. Rock magnetic, chemical and bacterial community analysis of a modern soil from Nebraska. Earth Planet. Sci. Lett. 251, 168–178.

Hall, A.J., 1986. Pyrite-pyrrhotine redox reactions in nature. Mineral. Mag. 50, 223–229.

Handler, R.M., Beard, B.L., Johnson, C.M., Scherer, M.M., 2009. Atom exchange between aqueous Fe(II) and goethite: An Fe isotope tracer study. Environ. Sci. Technol. 43, 1102–1107.

Hasenmueller, E.A., Gu, X., Weitzman, J.N., Adams, T.S., Stinchcomb, G.E., Eissenstat, D.M., Drohan, P.J., Brantley, S.L., Kaye, J.P., 2017. Weathering of rock to regolith: The activity of deep roots in bedrock fractures. Geoderma 300, 11–31.

Heller, M.I., Lam, P.J., Moffett, J.W., Till, C.P., Lee, J.M., Toner, B.M., Marcus, M.A., 2017. Accumulation of Fe oxyhydroxides in the Peruvian oxygen deficient zone implies non-oxygen dependent Fe oxidation. Geochim. Cosmochim. Acta 211, 174–193.

Herndon, E.M., Martínez, C.E., Brantley, S.L., 2014. Spectroscopic (XANES/XRF) characterization of contaminant manganese cycling in a temperate watershed. Biogeochemistry 121, 505–517.

Hilton, R.G., West, A.J., 2020. Mountains, erosion and the carbon cycle. Nat. Rev. Earth Environ. 1, 284–299.

Holmstrom, H., Ohlander, B., 2001. Layers rich in Fe- and Mn-oxyhydroxides formed at the tailings-pond water interface, a possible trap for trace metals in flooded mine tailings. J. Geochem. Explor. 74, 189–203.

Horng, C.S., Roberts, A.P., 2006. Authigenic or detrital origin of pyrrhotite in sediments?: Resolving a paleomagnetic conundrum. Earth Planet. Sci. Lett. 241, 750–762.

Hubbard, S.S., Williams, K.H., Agarwal, D., Banfield, J., Beller, H., Bouskill, N., Brodie, E., Carroll, R., Dafflon, B., Dwivedi, D., Falco, N., Faybishenko, B., Maxwell, R., Nico, P., Steefel, C., Steltzer, H., Tokunaga, T., Tran, P.A., Wainwright, H., Varadharajan, C., 2018. The East River, Colorado, watershed: A mountainous community testbed for improving predictive understanding of multiscale hydrological–biogeochemical dynamics. Vadose Zo. J. 17, 180061.

Kars, M., Aubourg, C., Suárez-Ruiz, I., 2015. Neoformed magnetic minerals as an indicator of moderate burial: The key example of middle Paleozoic sedimentary rocks, West Virginia. Am. Assoc. Pet. Geol. Bull. 99, 389–401.

Kim, Y.K., Son, H.Y., Choi, Y.S., Moon, K.-S., Sunwoo, K.H., 2000. Magnetically soft and electrically resistive CoNiFeS alloy films prepared by electrodeposition. J. Appl. Phys. 87, 5413.

Kimball, B.A., Runkel, R.L., Wanty, R.B., Verplanck, P.L., 2010. Reactive solute-transport simulation of pre-mining metal concentrations in mine-impacted catchments: Redwell Basin, Colorado, USA. Chem. Geol. 269, 124–136.

Kirschvink, J.L., Kopp, R.E., Raub, T.D., Baumgartner, C.T., Holt, J.W., 2008. Rapid, precise, and high-sensitivity acquisition of paleomagnetic and rock-magnetic data: Development of a low-noise automatic sample changing system for superconducting rock magnetometers. Geochem. Geophys. Geosyst. 9, Q05Y01.

Kissin, S., Scott, S., 1982. Phase relations involving pyrrhotite below 350 degrees C. Econ. Geol. 77, 1739–1754.

Kopp, R.E., Kirschvink, J.L., 2008. The identification and biogeochemical interpretation of fossil magnetotactic bacteria. Earth-Sci. Rev. 86, 42–61.

Kraft, S., Stümpel, J., Becker, P., Kuetgens, U., 1996. High resolution x-ray absorption spectroscopy with absolute energy calibration for the determination of absorption edge energies. Rev. Sci. Instrum. 67, 681–687.

Kump, L.R., Brantley, S.L., Arthur, M.A., 2000. Chemical weathering, atmospheric CO_2 and climate. Annu. Rev. Earth Planet. Sci. 28, 611–667.

Lagroix, F., Guyodo, Y., 2017. A new tool for separating the magnetic mineralogy of complex mineral assemblages from low temperature magnetic behavior. Front. Earth Sci. 5, 61.

Larrasoana, J.C., Roberts, R.J., Musgrave, R.J., Gracia, E., Pinera, E., Vega, M., Martinez-Ruiz, F., 2007. Diagenetic formation of greigite and pyrrhotite in gas hydrate marine sedimentary systems. Earth Planet. Sci. Lett. 261, 350–366.

Liu, Q., Yu, Y., Torrent, J., Roberts, A.P., Pan, Y., Zhu, R., 2006. Characteristic low-temperature magnetic properties of aluminous goethite [α-(Fe, Al) OOH] explained. J. Geophys. Res. Earth Surf. 111, B12S34.

Liu, Q., Roberts, A.P., Larrasoaña, J.C., Banerjee, S.K., Guyodo, Y., Tauxe, L., Oldfield, F., 2012. Environmental magnetism; principles and applications. Rev. Geophys. 50, RG4002.

Lovley, D.R., Stolz, J.F., Nord, G.L., Phillips, E.J., 1987. Anaerobic production of magnetite by a dissimilatory iron-reducing microorganism. Nature 330, 252.

Maher, B.A., 2011. The magnetic properties of Quaternary aeolian dusts and sediments, and their palaeoclimatic significance. Aeolian Res. 3, 87–144.

Maher, B.A., Karloukovski, V., Mutch, T., 2004. High-field remanence properties of synthetic and natural submicrometre haematites and goethites: significance for environmental contexts. Earth Planet. Sci. Lett. 226, 491–505.

Maher, B.A., Taylor, R.M., 1988. Formation of ultrafine-grained magnetite in soils. Nature 336, 368.

Maher, B.A., Thompson, R., 1992. Paleoclimatic Significance of the Mineral Magnetic Record of the Chinese Loess and Paleosols. Quat. Res. 170, 155–170.

Manceau, A., Tamura, N., Marcus, M.A., MacDowell, A.A., Celestre, R.S., Sublett, R.E., Sposito, G., Padmore, H.A., 2002. Deciphering Ni sequestration in soil ferromanganese nodules by combining X-ray fluorescene, absorption, and diffraction at micrometer scales of resolution. Am. Mineral. 87, 1494–1499.

Manning, A.H., Verplanck, P.L., Caine, J.S., Todd, A.S., 2013. Links between climate change, water-table depth, and water chemistry in a mineralized mountain watershed. Appl. Geochem. 37, 64–78.

Manning, A.H., Ball, L.B., Wanty, R.B., Williams, K.H., 2020. Direct observation of the depth of active groundwater circulation in an alpine watershed. Water Resour. Res. 57, WR028548.

Marcus, M.A., MacDowell, A.A., Celestre, R., Manceau, A., Miller, T., Padmore, H.A., Sublett, R.E., 2004. Beamline 10.3.2 at ALS: A hard X-ray microprobe for environmental and materials sciences. J. Synchrotron Radiat. 11, 239–247.

Mast, M.A., Turk, J.T., Clow, D.W., Campbell, D.H., 2011. Response of lake chemistry to changes in atmospheric deposition and climate in three high-elevation wilderness areas of Colorado. Biogeochemistry 103, 27–43.

Maxbauer, D.P., Feinberg, J.M., Fox, D., 2016. MAX UnMix: A web application for unmixing magnetic coercivity distributions. Comput. Geosci. 95, 140–145.

Meybeck, M., 1987. Global chemical weathering of surficial rocks estimated from river dissolved loads. Am. J. Sci. 287, 401–428.

Moncur, M.C., Jambor, J.L., Ptacek, C.J., Blowes, D.W., 2009. Mine drainage from the weathering of sulfide minerals and magnetite. Appl. Geochem. 24, 2362–2373.

Moore, D.M., Reynolds, R.C., 1997. X-ray diffraction and identification and analysis of clay minerals. Oxford University, New York.

Morin, F., 1950. Magnetic susceptibility of αFe2O3 and αFe2O3 with added titanium. Phys. Rev. 78, 819–820.

Muñoz, M., De Andrade, V., Vidal, O., Lewin, E., Pascarelli, S., Susini, J., 2006. Redox and speciation micromapping using dispersive X-ray absorption spectroscopy: Application to iron in chlorite mineral of a metamorphic rock thin section. Geochem. Geophys. Geosyst. 7, Q11020.

Nordstrom, D.K., 2011. Hydrogeochemical processes governing the origin, transport and fate of major and trace elements from mine wastes and mineralized rock to surface waters. Appl. Geochem. 26, 1777–1791.

Ozdemir, O., Dunlop, D.J., 2010. Hallmarks of maghemitization in low-temperature remanence cycling of partially oxidized magnetite nanoparticles. J. Geophys. Res. Earth Surf. 115, B02101.

Pannalal, S.J., Crowe, S.A., Cioppa, M.T., Symons, D.T., Sturm, A., Fowle, D.A., 2005. Room-temperature magnetic properties of ferrihydrite: A potential magnetic remanence carrier? Earth Planet. Sci. Lett. 236, 856–870.

Parviainen, A., Cruz-Hernández, P., Pérez-López, R., Nieto, J.M., Delgado-López, J.M., 2015. Raman identification of Fe precipitates and evaluation of As fate during phase transformation in Tinto and Odiel River Basins. Chem. Geol. 398, 22–31.

Peak, D., Sparks, D.L., 2002. Mechanisms of selenate adsorption on iron oxides and hydroxides. Environ. Sci. Technol. 36, 1460–1466.

Peter, C., Dekkers, M., 2003. Selected room temperature magnetic parameters as a function of mineralogy, concentration and grain size. Phys. Chem. Earth, Parts A/B/C 28, 659–667.

Post, J.E., 1999. Manganese oxide minerals: Crystal structures and economic and environmental significance. Proc. Natl. Acad. Sci. U. S. A. 96, 3447–3454.

Potter, D., Stephenson, A., 1986. The detection of fine particles of magnetite using anhysteretic and rotational remanent magnetizations. GeoJI 87, 569–582.

Putz, H., Brandenburg, K., 2011. Match! - Phase identification from powder diffraction. Cristal Impact. 137.

Ravel, B., Newville, M., 2005. ATHENA, ARTEMIS, HEPHAESTUS: data analysis for X-ray absorption spectroscopy using IFEFFIT. J. Synchrotron Radiat. 12, 537–541.

Rochette, P., Fillion, G., Mattie, J.-L., Dekkers, M., 1990. Magnetic transition at 30–34 Kelvin in pyrrhotite: Insight into a widespread occurrence of this mineral in rocks. Earth Planet. Sci. Lett. 98, 319–328.

Rosera, J.M., Gaynor, S.P., Coleman, D.S., 2021. Spatio-temporal shifts in magmatism and mineralization in Northern Colorado beginning in the late eocene. Econ. Geol. 116, 987–1010.

Seedorff, E., Diller, J.H., Proffett, J.M.J., Einaudi, M.T., Zurcher, L., Stavast, W.J.A., Johnson, D.A., Barton, M.D., 2005. Porphyric deposits: characteristics amd origin of hypogene feature. Econ. Geol. 100, 251–298.

Sharp, J.E., 1978. A molybdenum mineralized breccia pipe complex, Redwell Basin, Colorado. Econ. Geol. 73, 369–382.

Sherman, D.M., Randall, S.R., 2003. Surface complexation of arsenic(V) to iron(III) (hydr)oxides: Structural mechanism from ab initio molecular geometries and EXAFS spectroscopy. Geochim. Cosmochim. Acta 67, 4223–4230.

Slotznick, S.P., Swanson-Hysell, N.L., Sperling, E.A., 2018. Oxygenated Mesoproterozoic lake revealed through magnetic mineralogy. Proc. Natl. Acad. Sci. U. S. A. 115, 12938–12943.

Slotznick, S.P., Webb, S.M., Kirschvink, J.L., Fischer, W.W., 2019. Mid-Proterozoic ferruginous conditions reflect postdepositional processes. Geophys. Res. Lett. 46, 3114–3123.

Snowball, I.F., 1997. The detection of single-domain greigite (Fe3S4) using rotational remanent magnetization (RRM) and the effective gyro field (Bg): mineral magnetic and palaeomagnetic applications. GeoJI 130, 703–716.

Sullivan, P.L., Hynek, S.A., Gu, X., Singha, K., White, T., West, N., Kim, H., Clarke, B., Kirby, E., Duffy, C., Brantley, S.L., 2016. Oxidative dissolution under the channel leads geomorphological evolution at the shale hills catchment. Am. J. Sci. 316, 981–1026.

Sullivan, P.L., Goddéris, Y., Shi, Y., Gu, X., Schott, J., Hasenmueller, E.A., Kaye, J., Duffy, C., Jin, L., Brantley, S.L., 2019. Exploring the effect of aspect to inform future earthcasts of climate-driven changes in weathering of shale. J. Geophys. Res. Earth Surf. 124, 974–993.

Suzuki, Y., Kopp, R.E., Kogure, T., Suga, A., Takai, K., Tsuchida, S., Ozaki, N., Endo, K., Hashimoto, J., Kato, Y., 2006. Sclerite formation in the hydrothermal-vent ‘‘scaly-foot" gastropod—possible control of iron sulfide biomineralization by the animal. Earth Planet. Sci. Lett. 242, 39–50.

Swanson-Hysell, N.L., Maloof, A.C., Kirschvink, J.L., Evans, D.A.D., Halverson, G.P., Hurtgen, M.T., 2012. Constraints on neoproterozoic paleogeography and paleozoic orogenesis from paleomagnetic records of the bitter springs formation, amadeus basin, central Australia. Am. J. Sci. 312, 817–884.

Taylor, K.G., Macquaker, J.H.S., 2014. Diagenetic alterations in a silt- and clay-rich mudstone succession: an example from the Upper Cretaceous Mancos Shale of Utah, USA. Clay Miner. 49, 213–227.

Thomas, J.A., Galey, J.T., 1982. Exploration and geology of the Mt. Emmons molybdenite deposits, Gunnison County, Colorado. Econ. Geol. 77, 1085–1104.

Thomson, G.F., 1990. The anomalous demagnetization of pyrrhotite. GeoJI 103, 425–430.

Toner, B.M., Rouxel, O.J., Santelli, C.M., Bach, W., Edwards, K.J., 2016. Iron transformation pathways and redox micro-environments in seafloor sulfide-mineral deposits: Spatially resolved Fe XAS and δ57/54Fe observations. Front. Microbiol. 7, 648.

Tuttle, M.L.W., Fahy, J.W., Elliott, J.G., Grauch, R.I., Stillings, L.L., 2014. Contaminants from Cretaceous black shale: I. Natural weathering processes controlling contaminant cycling in Mancos Shale, southwestern United States, with emphasis on salinity and selenium. Appl. Geochem. 46, 57–71.

Tweto, O., Sims, P.K., 1963. Precambrian ancestry of the Colorado Mineral Belt. GSA Bull. 78, 991–1014.

Verplanck, P.L., Wanty, R.B., Berger, B.R., Tuttle, M.L., Kimball, B.A., Farmer, G.L., 2004. Hydrogeochemistry of an acidic, alpine watershed, Redwell Basin, Colorado. Proc. - Int. Symp. Water-Rock Interact. 11, 1649–1653.

Verplanck, P.L., Nordstrom, D.K., Bove, D.J., Plumlee, G.S., Runkel, R.L., 2009. Naturally acidic surface and ground waters draining porphyry-related mineralized areas of the Southern Rocky Mountains, Colorado and New Mexico. Appl. Geochem. 24, 255–267.

Verwey, E., 1939. Electronic conduction of magnetite (Fe3O4) and its transition point at low temperatures. Nature 144, 327–328.

Wanty, R.B., Verplanck, P.L., Tuttle, M.L., Runkel, R.L., Berger, B.R., Kimball, B.A., 2004. Resolving natural and anthropogenic sources of solutes to a watershed from historic mining. Proc. - Int. Symp. Water-Rock Interact. 11, 1659–1663.

Waychunas, G.A., Kim, C.S., Banfield, J.F., 2005. Nanoparticulate iron oxide minerals in soils and sediments: Unique properties and contaminant scavenging mechanisms. J. Nanoparticle Res. 7, 409–433.

Webb, S.M., 2011. The Microanalysis toolkit: X-ray fluorescence image processing software. In: AIP Conference Proceedings, pp. 196–199.

West, A.J., Galy, A., Bickle, M., 2005. Tectonic and climatic controls on silicate weathering. Earth Planet. Sci. Lett. 235, 211–228.

Williams, A.G.B., Scherer, M.M., 2004. Spectroscopic evidence for Fe(II)-Fe(III) electron transfer at the iron oxide-water interface. Environ. Sci. Technol. 38, 4782–4790.